Doctor of Philosophy Thesis

First-Principles Study on Electronic and Optical Properties of Ferromagnetic/Noble Metal Multilayers and Its Application to Surface Plasmon Resonance

Muhammad Arifin

MIE UNIVERSITY

Graduate School of Engineering

Division of Materials Science

March 2022

Doctor of Philosophy Thesis

First-Principles Study on Electronic and Optical Properties of Ferromagnetic/Noble Metal Multilayers and Its Application to Surface Plasmon Resonance

強磁性金属/貴金属多層膜の電子構造と光学的性質の第一原理計算と表面プラズモン共鳴への応用

Muhammad Arifin

MIE UNIVERSITY

Graduate School of Engineering

Division of Materials Science

March 2022

Abstract

Optical sensors based on surface plasmon resonance (SPR) have advantages in measuring refractive index of material towards a development of highly sensitive biosensing sensors. Since the SPR-based sensors are limited in measuring chemical quantities such as concentrations of constituents, recent efforts have focused to utilize magneto-optical SPR (MOSPR), which combines magneto-optical Kerr effect (MOKE) to the SPR by using a hybrid magneto-plasmonic system consisting of ferromagnetic and noble metal thin films. With this background, the present dissertation devotes theoretical investigation of the electronic and optical properties of ferromagnetic/noble metal multilayers, based on first-principles calculations, and proposes a guideline for highly sensitive MOSPR sensors in term of material design.

The dissertation consists of six chapters. Chapter one states the basic concept of SPR and MOSPR, and presents purpose of study. Chapter two describes methodologies of calculations. First, method of electronic structure calculations based on density functional theory are presented where calculations are performed by using full-potential linearized augmented plane wave method. Second, the macroscopic and microscopic theories of the magneto-optical Kerr effect (MOKE) are presented. The optical conductivity tensors are calculated by applying the Kubo formula in the linear response theory and the reflectivities of multilayer systems are evaluated based on 4×4 transfer matrix method.

Chapter three provides systematically results of optical properties for transition metals, 3*d* (Fe, Ni, Co, Cu), 4*d* (Ru, Rh, Pd, Ag), and 5*d* (Os, Ir, Pt, Au) metals, by first-principles calculations. The transition metals, especially noble metals, are known to be desired candidates to plasmonic materials as used in sensing layers of the SPR applications. To clarify these optical characteristics, we calculated the optical conductivities and dielectric functions. Results for all systems can be reproduced to experimental trends. The edge position of the real part of diagonal optical conductivity of 1.7, 2.9, and 1.8 eV for Cu, Ag, and Au, respectively, can be confirmed by the band-by-band decomposition analysis proposed in the present study. We find that calculated SPR reflectivity curves of the noble metals in the Kretschmann configuration demonstrate sharp dips that correspond to small values of the imaginary parts of the dielectric functions.

In chapter four, the investigation is extended to apply ferromagnetic/noble metal multilayers, Fe_xCu_x superlattices (SLs) with x = 1, 2, and 3. One of the main physical quantities in magnetoplasmonic is the optical loss caused by the dipole-interband transitions. From calculated electronic structures of Fe_xCu_x SLs, we find that the interband transitions responsible in the optical losses that can be tuned through orbital hybridization by varying the thickness of the superlattices. In the visible range, Fe_xCu_x SLs are found to have excellent magnetoplasmonic properties, indicated by negative real part of diagonal component of dielectric tensor and by non-zero off-diagonal component, which promise to martial candidates in the MOSPR applications. In addition, the electronic origin in the optical and magneto-optical anisotropies (OA and MOA) of the Fe_1Cu_1 SLs can be elucidated by the band-by-band decomposition analysis.

In chapter five, the MOSPR system with Fe_xCu_x SLs as a magnetoplasmonic structure is proposed, where the TMOKE is employed in the Kretschmann configuration. The results show that a crossing position with respect to SPR angle between reflectivity curves for the positive and negative applied magnetization gives the strength of the TMOKE signal. Consequently, the maximum slopes of TMOKE signals results in 0.31, 1.00, and 12.23 /degree for Fe_xCu_x SLs with x = 1, 2, and 3, respectively. To concreting the MOSPR system by using Fe_xCu_x SLs, when a small variation of the refractive index of a gelatin is introduced, the sensitivity in the MOSPR system is enhanced to 600.1 RIU^{-1} for Fe_3Cu_3 SL, which is two order of magnitude higher than that of the SPR system. Thus, the ferromagnetic/noble metal superlattice structure is promising choice to demonstrate high performance in the MOSPR applications.

Chapter six remarks conclusions and prospects of the present study.

Acknowledgments

Alhamdulillah, All praise be to the Lord.

I owe a great deal of gratitude to Professor Kohji Nakamura, my supervisor, who has given me the opportunity to conduct my Ph.D. at the Graduate School of Engineering, Mie University. His patience, knowledge, guidance, understanding, and great support have helped me to complete my study and thesis writing. Various opportunities to participate in workshops and conferences with his support have upgraded my experience as a researcher.

I am grateful to my committee members for their patience and comments during my thesis defense, Professors Kohji Nakamura, Kazuhiro Sano, Hiroshi Murata, and Hiroshi Yao at the Graduate School of Engineering, Mie University.

My sincere thanks go to Professors Tomonori Ito and Toru Akiyama at the Graduate School of Engineering, Mie University, for their kind help and advice during my study. I would like to thank also to Dr. Kenji Nawa at the Graduate School of Engineering, Mie University, for many discussions and suggestions. I would also like to thank personally to Dr. Abdul Muizz Tri Pradipto at the Faculty of Mathematics and Natural Sciences, Bandung Institute of Technology, Indonesia. His discussion, support, and guidance really played an important role in my research work.

I would like to thank also to the whole team of the MAGN group. Thank you so much for all of your discussions and support. I also would like to thank my Indonesian friends in Japan, especially the Indonesian Student Association Mie (PPI Mie), for their spirit and support.

I am thankful to the Japanese Government for their generous financial support through the Monbukagakusho: MEXT Scholarship.

Finally, for their encouragement throughout my studies, I would like to thank all my family for their prayers and support during my study. Special mention goes to my wife (Transista Condensi) and my children (Husna Huwaidah Muthmainnah and Muhammad Hanif Akira) for their consistent love, patience, and support that made finishing this thesis possible.

March 2022,

Muhammad Arifin

Contents

List of Tables

List of Figures

Chapter 1

Introduction

1.1 Background

Interest in surface plasmon resonance (SPR) has rapidly increased in optical sensing applications, including biosensing [1,2], bioimaging [3,4], colorimetric sensor [5,6], disease detection [7–9], environmental monitoring [10,11], food safety [12–14], and medical diagnosis [15,16]. This is a phenomenon associated with surface plasmons polaritons (SPPs), which can be excited by light at metal/dielectric interfaces. [17] Several methods are used to excite the SPP, including prism-, grating-, and waveguide coupler methods. [18] The prism coupling method, schematically shown in Fig. 1.1, has been used as a standard configuration based on the Kretschmann configuration [19]. The first experimental demonstration as sensing was reported by Liedberg and co-workers in 1983. [20]

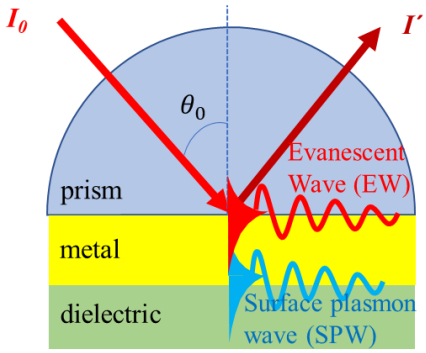

Figure 1.1: Schematic diagram of SPR structure in the Kretschmann configuration.

The SPR refers to a condition where there is a resonance between evanescent waves at a prism/metal interface and surface plasmon waves at a metal/dielectric interface (see Fig.1.1). The wavevector of the evanescent wave propagating along the prism/metal interface is given by

$$k_{EW} = \frac{2\pi}{\lambda}\sqrt{\varepsilon_p}\sin(\theta_0), \tag{1.1}$$

where ε_p is a dielectric function of the prism, θ_0 is an incident angle, and λ is a wavelength of the incident light. The wavevector of the surface plasmon wave along the metal/dielectric interface is

$$k_{SPW} = \frac{\omega}{c}\sqrt{\frac{\varepsilon_m \varepsilon_d}{\varepsilon_m + \varepsilon_d}}, \tag{1.2}$$

where ω is an angular frequency of wave, c is the speed of light in vacuum, ε_m and ε_d are dielectric functions of the metals and dielectric, respectively. The resonance condition is thus occurred when $k_{EW} = k_{SPW}$, and the SPR angle at the resonance condition can be given by

$$\theta_{SPR} = \sin^{-1}\left(\sqrt{\frac{1}{\varepsilon_p}\frac{\varepsilon_m \varepsilon_d}{\varepsilon_m + \varepsilon_d}}\right). \tag{1.3}$$

Variation in the dielectric function of dielectric media may lead to a change in the SPP wavevector of Eq. 1.2, which alters directly the resonance condition. This feature is the foundation of the SPR sensors, and thus a high sensitivity in the SPR sensor can be achieved so that a significant shift in a SPR angle or a SPR wavelength is yielded by a small change in the refractive index at the close vicinity of the sensing layer.

The performance factor of the sensor is generally represented by the limit of detection (LOD), namely, the smallest concentration or quantity measured by output signals. It is given by LOD = $3\sigma/S$, where σ is a standard deviation, and S is a sensitivity of the sensor. As noted above, the sensitivity is determined by the resonance shift with respect to the change of the refractive index of a dielectric. Since the sensitivity is determined by a slope of the reflectivity curve, many efforts have been focused on a design of sensing structures including materials.

The development of SPR sensors in biosensor applications has been marked by the emergence of several commercially available instruments, like BIAcore, IBIS, SPR-670, IASys, BioNavis, and others. The first commercial SPR sensor was launched in 1990 by BIAcore, based on the Kretschmann configuration and angular modulation. Since then, the instruments have evolved, and several new manufacturers provide SPR instruments with new features. However, research involving SPR sensors based on the Kretschmann configuration continues to date. Table 1.1 summarizes the state of the art on performance of prism-based SPR sensors in the Kretschmann configuration.

Table 1.1 State of the art on SPR sensor in the Kretschmann configuration.

Year	Sensing layer	Target sample	Performance	Reference
1983	Ag	Antibody human γ-globulin	-	[20]
2010	Ti/Au	Bovine serum albumin	LOD: 2.5×10^{-6} RIU	[21]
2014	Ag nanorod	Glucose	LOD: 7.1×10^{-8} RIU	[22]
2015	Au/ succinimidyl-terminated propanethiol monolayer	Dithiobis(succinimidyl) propionate	LOD: 3 pg/mL (3 ppt)	[23]
2016	Au/SnO_2	Amonia gas	Sensitivity: 0.055°/ppm	[10]
2016	Au/ZnO/ssDNA	DNA of *Neisseria meningitidis*	Sensitivity: 0.03°/(ng/μl)	[24]
2017	Bimetalic Ag/Au	VP1 protein	LOD: 4.8 pg/mL	[25]
2017	SiO_2/Au	Water	LOD: 6.79×10^{-5} RIU	[26]
2018	Molecularly imprinted polymer nanoparticles	α-casein	LOD: 127 ng/mL (0.127 ppm)	[27]
2019	Modified-nanocrystalline cellulose/graphene oxide	Zinc ion	LOD: 0.01 ppm	[28]
2020	Cr/Au	Carbon dioxide	Sensitivity: 6640 %/RIU	[11]
2021	Bimetallic Ag-Au	Cathepsin S protein	LOD: 0.031 ng/mL	[29]

*RIU: refractive index unit

Previously, we carried out experiments by using the conventional SPR sensors to detect gelatins with two concentrations of 1% and 2.5% based on the Kretschmann configuration. [30] Due to the low sensitivity of the present SPR setup, however, the two concentrations could not be distinguished. We further improved the accuracy of the SPR setup, and the built system had been successfully demonstrated to increase the resolution of an incident angle by 0.01°. [31] By reconstructing the detection method additionally, the LOD of the sensor to the bovine and porcine gelatins resulted in 0.22% (w/w). [32] Because food products with porcine-derived gelatins are not acceptable in Muslim communities, the development toward high sensitive SPR sensors in analyzing gelatins is one of highlights.

Efforts towards highly sensitive SPR sensors have been further made to utilize magneto-optical SPR (MOSPR) phenomena, which combines a magneto-optical Kerr effect (MOKE) to the SPR phenomena by using hybrid magnetoplasmonic materials. The phenomenon of MOSPR is schematically illustrated in Fig. 1.2. In contrast to conventional SPR, the MOSPR configuration uses a sensing layer in a combination of magnetic and plasmonic materials in an external magnetic field along to the in-plane direction. In the magnetoplasmonic system, magnetic and plasmonic properties are intertwined, allowing the control of plasmonic properties by external magnetic field or magnetization directions, so-called magneto-optical (MO) activity. [33,34] Althoguh ferromagnetic metals exhibit large optical losses and very broad plasmon resonances in the visible range, they may enable high MO activity, while noble metals, characterized by their low optical losses, support propagating surface plasmon modes. Particularly, the MOSPR sensors utilizing the transverse magneto-optical Kerr effect (TMOKE) have been developed to date. [26,33,35–40] In this configuration, a magnetic field is applied perpendicular to the plane of incident light, where the TMOKE signal can be characterized by relative changes in the reflectivity of light when the magnetization direction is reversed.

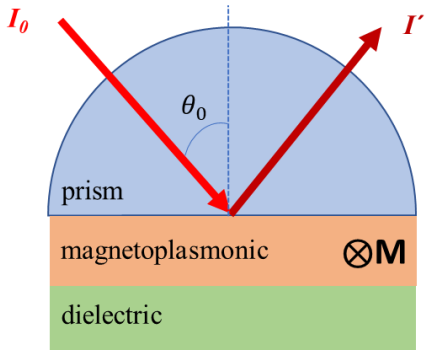

Figure 1.2: Schematic illustration of magnetoplasmonic structure in the Kretschmann configuration. A magnetic field is applied perpendicular to the incident plane.

Recently, Qin *et al.* [26] demonstrated the TMOKE experiments using low loss magneto-optical oxide thin films, and the LOD reaches 4.13×10^{-6} RIU (refractive index unit), which is higher by a factor of 16 compared to a standard Au SPR sensor. Rizal *et al.* [39] reported the response of the SPR and TMOKE signals in magneto-optic plasmonic nanostructures using Ti/Au(Ag)/Co/Au. The sensitivity of the MOSPR sensor was improved by three times over the ordinal SPR sensitivity. Theoretical studies are also proposed to demonstrate a giant enhancement of TMOKE signal and a high sensitivity of

MOSPR sensors. For example, Moncada-villa *et al*. [41] theoretically predicted a negative peak of the maximum value of TMOKE (~ −1), using uniaxial ε-near-zero metamaterial on Fe substrate, with the sensitivity of 11.55 °/RIU. Wang *et al*. [42] also theoretically investigated the sensing performance of MOSPR sensor in CoFeB slab coupled with an Au grating and showed the sensitivity of 105 °/RIU. The study has been extended to multilayer and nanostructure systems [43,44] that we have interested in the present work, in which superlattices (SLs) are found to have an advantage that offers a wide range of customizable properties because of the flexibility in material selections.

1.2 Purpose of study

The present thesis has mainly two objectives; origins in optical and MO properties of the FM/NM SL and sensitivity of the MOSPR sensors. For this, we calculated the optical conductivity tensors of the sensing layers based on density functional theory (DFT). We first look at transitions metals systematically according to the periodic table, and then we expand our investigations to a multilayer system of FeCu SLs. Finally, we demonstrate the sensitivity of the MOSPR sensor using FeCu SLs in the Kretschmann configuration.

The thesis is organized as follows. Chapter one presents the basic concept of SPR and MOSPR sensors and the purpose of the present work. In chapter two, we describe DFT and full potential augmented plane wave (FLAPW) method for calculating electronic structures of the sensing layers, and we present theory of optical and MO properties. In chapter three, we present calculated results of optical properties of transition metals and reflectivity curves in the Kretschmann configuration. In chapter four, we present results of the optical and MO properties of the FeCu SLs, including optical and MO anisotropies (OA and MOA). In chapter five, we present results of the TMOKE signal in the FeCu SLs and discuss the sensitivity of the MOSPR sensor. In chapter six, we summarize the present work.

Chapter 2

Theory and methods

2.1 Electronic structure calculations

2.1.1 Density functional theory

The condensed matter physics has a rich diversity of physical phenomena, which has been well studied experimentally and theoretically, in while computer modeling and simulation have emerged as indispensable methods for the research of materials. Since condensed matter systems are made of many atoms consisting of positively charged nuclei surrounded by one or more negatively charged electrons, physical properties may be understood by identifying the interactions of their constituent electrons and nuclei. According to quantum mechanics principles, the many-body Schrödinger equation is given by

$$H\Psi(\{\mathbf{r}_i, \mathbf{R}_I\}) = E\Psi(\{\mathbf{r}_i, \mathbf{R}_I\}) \tag{2.1}$$

where $\Psi(\{\mathbf{r}_i,\mathbf{R}_I\})$ is a wavefunction of the system, $\mathbf{r}_i$ and $\mathbf{R}_I$ are the coordinators of *i*-th electron and *I*-th nucleus, respectively, and *E* is the total energy of the system. *H* is the Hamiltonian of the system, defined in atomic units as [45]

$$H = -\sum_i \frac{\nabla_i^2}{2} - \sum_I \frac{\nabla_I^2}{2M_I} + \frac{1}{2}\sum_i \sum_{j\neq i} \frac{1}{|\mathbf{r}_i - \mathbf{r}_j|}$$
$$-\sum_i \sum_I \frac{Z_I}{|\mathbf{r}_i - \mathbf{R}_I|} + \frac{1}{2}\sum_i \sum_{J\neq I} \frac{Z_I Z_J}{|\mathbf{R}_I - \mathbf{R}_J|}. \tag{2.2}$$

where M_I and Z_I are the mass and charge of the *I*-th nucleus. We can write the Hamiltonian in Eq. (2.2) as:

$$H = T_{el} + T_{nuc} + U_{el-el} + U_{el-nuc} + U_{nuc-nuc}. \tag{2.3}$$

The first and second terms are the kinetic energy operators of electrons and nuclei, respectively. Other terms are Coulomb interactions between electrons and electrons, electrons and nuclei, and nuclei and nuclei, respectively. In the Born-Oppenheimer approximation, the electronic motion and the nuclei motion can be separated. The physical basis for the Born-Oppenheimer approximation is the fact that the nuclei are several thousand times heavier than the electrons.

There are two traditional methods for solving the many-body Schrodinger equation, namely the Hartree and Hartree-Fock approximation. The Hartree approximation is a simple approximation that starts with the one-electron equation. The Hartree-Fock approximation is a method which considers anti-symmetric of the wavefunction in terms of a Slater determinant written using one-electron Schrödinger wavefunctions. The Hartree-Fock methods neglect proper Coulomb correlations but only include correlations among the positions of electrons with parallel spin due to the Pauli principle. In contrast, density functional theory (DFT) is an alternate method for solving the many-body Schrödinger equation, based on the electron density rather than the many-body wavefunction. This method was introduced by Hohenberg and Kohn in 1964 [46] that ground-state properties of a many-electron system can be determined by a functional depending only on the density distribution. Kohn and Sham then perfected the DFT method in 1965 [47] and showed how to replace the many-body problem with a self-consistent one-electron equation by adding the effective potential to incorporate the many-body effect.

We focus on the electron density, which is defined as:

$$n(\mathbf{r}) = \langle \Psi | \hat{n}(\mathbf{r}) | \Psi \rangle, \tag{2.4}$$

where $\hat{n}(\mathbf{r})$ is the electron density operator, given by:

$$\hat{n}(\mathbf{r}) = \sum_i \delta(\mathbf{r} - \mathbf{r}_i)\,. \tag{2.5}$$

There are two basic theorems introduced by Hohenberg and Kohn to describe electron density.

Theorem 1 *The external potential $V_{ext}(\mathbf{r})$ is determined uniquely for any many-electron system by the ground-state electron density $n(\mathbf{r})$.*

Theorem 2 *A universal functional for the total energy $E[n]$ in terms of the density $n(r)$ can be defined, valid for any external potential $V_{ext}(\mathbf{r})$. The exact ground state energy of the system is the global minimum of this functional, and the density that minimizes the functional is the exact ground state density $n_0(\mathbf{r})$.*

The first theorem indicates that the exact ground-state electron determines all ground-state properties, and the second theorem implies that the kinetic $T[n]$ and interacting energies $E_{int}[n]$ are the functionals of electron density. The total energy is given by (ignoring the nuclei-nuclei interaction):

$$E[n] = T[n] + E_{int}[n] + \int n(\mathbf{r}) V_{ext}(\mathbf{r}) \mathrm{d}\mathbf{r}\,. \tag{2.6}$$

The Kohn-Sham method is a suitable formulation of DFT to solve Eq. (2.6). This method used the variational principle implied by the minimal properties of the energy functional to derive a single-particle Schrödinger equation. In this method, the ground state density is assumed in the non-interacting system, which is given by:

$$n(\mathbf{r}) = \sum_{i}^{N} \left|\psi_i(\mathbf{r})\right|^2 . \tag{2.7}$$

The Kohn-Sham equation is derived as:

$$\left(-\frac{\nabla^2}{2} + V_{KS}(\mathbf{r})\right)\psi_i(\mathbf{r}) = \epsilon_i \psi_i(\mathbf{r}), \tag{2.8}$$

where V_{KS} is Kohn-Sham potential, which is given as:

$$V_{KS}(\mathbf{r}) = V_{ext}(\mathbf{r}) + V_H(\mathbf{r}) + V_{xc}(\mathbf{r}). \tag{2.9}$$

The V_{ext}, V_{H}, and V_{xc} represent the external, Hartree, and exchange-correlation potentials, respectively. The solution for the Kohn-Sham equation is achieved from the self-consistent calculations schematically given in Fig. 2.1. At the beginning of the calculation, the initial electron density, obtained by a superpoition of atomic electron deinsty distribution, is made to calculate the Kohn-Sham potential V_{KS}. Subsequently, the Kohn-Sham equation is solved. From the eigenvalues and eigenfunctions, the total energy and new charge density are obtained. If there are not converged, the new guest of electron density is used to calculate the new V_{KS}. This procedure is then repeated until convergence is reached.

There are many approximations to approximate the exchange-correlation potential V_{xc} part. The simplest and most frequently used is the local density approximation (LDA). In this approximation, the exchange-correlation charge density $\rho_{xc}(\mathbf{r},\mathbf{r}'-\mathbf{r})$ has a form for a homogeneous electron gas, but with the density at every point of the space replaced by the local value of the charge density $\rho(\mathbf{r})$. However, LDA fails in situations where the density undergoes rapid changes. Therefore, the gradient of the electron density should be included. This approach is called the gradient-expansion approximation (GGA).

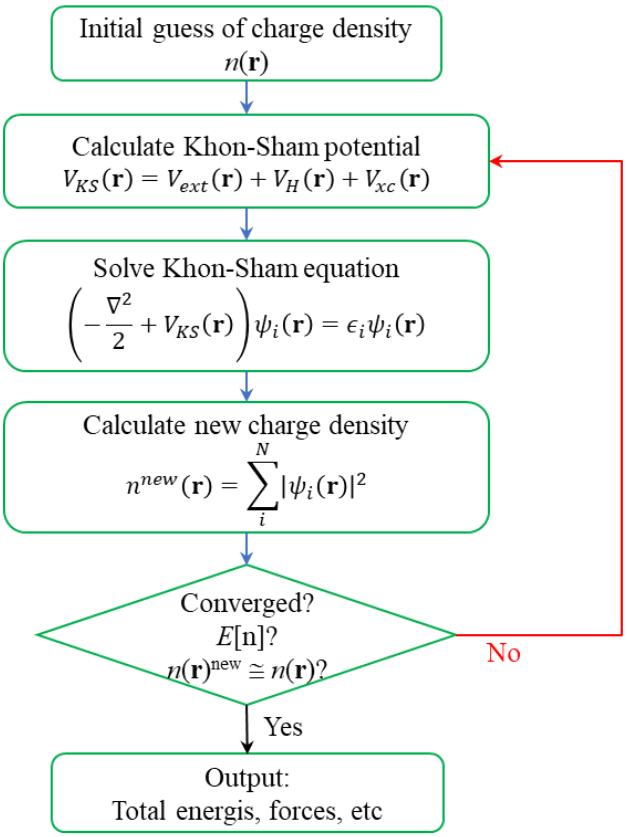

Figure 2.1: Self-consistent calculation for solving the Kohn-Sham equation.

2.1.2 Full-potential linearized augmented plane wave method

There are many possible ways to solve the Kohn-Sham equations. In order to solve the Kohn-Sham equations for periodic crystals systems, a set of plane waves is chosen as a basis function for the wavefunction satisfying the Bloch boundary condition. In the augmented plane-wave (APW) methods, which is proposed by Slater [48], the unit cell is divided into two different regions: one is a sphere region called the muffin tin (MT) region, and the remaining region is called the interstitial region. The disadvantage of the APW methods is that the wavefunction is energy-dependent, which leads to a nonlinear eigenvalue problem. In order to solve this problem, Andersen [49], Koelling and Arbman [50] proposed the linear APW (LAPW) method. The idea of the LAPW methods is to add extra variational freedom to the basis inside the muffin-tins by using the Taylor expansion of a radial function. The LAPW methods are difficult to apply for crystals with

open structures such as perovskites or surfaces. Both APW and LAPW methods employed shape-approximation on the potential used in the Hamiltonian.

The full-potential LAPW method (FLAPW), developed by Hamman and Wimmer [51,52], combines the choice of the LAPW basis set with the treatment of the charge density and full-potential without any shape-approximations inside the muffin-tin spheres and interstitial region. This generalization is achieved by relaxing the interstitial potential V_I^0 and the spherical muffin-tin approximation $V_{MT}^0(r)$ due to the inclusion of warped interstitial $\sum V_I^{\mathbf{G}} e^{i\mathbf{Gr}}$ and the non-spherical term inside the muffin-tin spheres: [53]

$$V(\mathbf{r}) = \begin{cases} \sum_G V_I^G e^{i\mathbf{Gr}} & \text{interstitial region} \\ \sum_L V_{MT}^L(r) Y_L(\hat{\mathbf{r}}) & \text{muffin-tin.} \end{cases} \tag{2.10}$$

Here, **G** are all reciprocal lattice vectors up to the largest value of $K_{\max}$, L abbreviates the quantum numbers l and m, and Y_L is the spherical harmonics. The FLAPW method is the method of choice for accurate electronic structure calculations. The code that has been used in this work is a FLAPW code developed by Nakamura and co-workers. [54]

2.2 Magneto-optical Kerr effect

2.2.1 Basic configurations

The MOKE, discovered by John Kerr in 1877, is a phenomenon in which the modification of polarization in reflected light on magnetized material, [55] which is widely used as potential applications such as biosensors [56], data storages [57], magnetometry [58], and spintronic devices [59]. Three geometries in the MOKE measurements, i.e., polar, longitudinal, and transversal geometries, have been configured depending on magnetization directions in a sample film with respect to the wave propagation direction and the surface normal, systematically shown in Fig. 2.2. [60] When the magnetization **M** is perpendicular to the sample surface, this phenomenon is called polar MOKE (PMOKE). If **M** is parallel to the surface and in the plane of incidence, it is called longitudinal MOKE (LMOKE). Finally, when **M** is parallel to the surface but perpendicular to the plane of incidence, this method is called transverse MOKE (TMOKE).

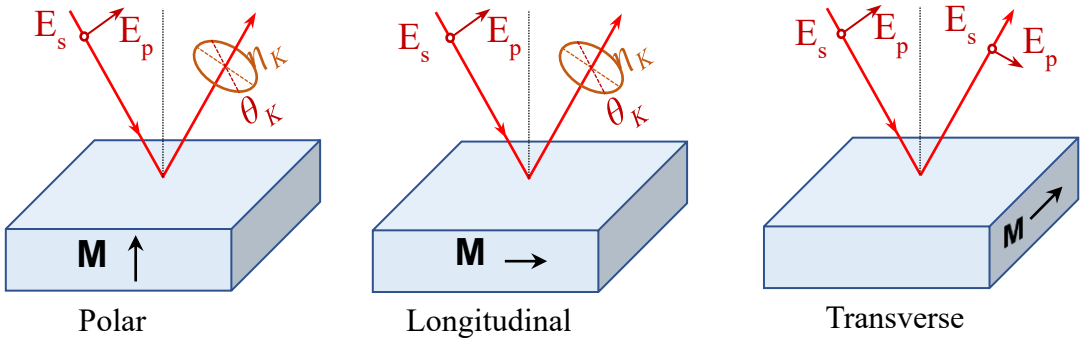

Figure 2.2: Illustration of the (a) polar, (b) longitudinal, and (c) transverse MOKE. The incident light is linear *p*- or *s*-polarized according to whether its *E*-fields are in the plane of incidence (E_p) or perpendicular to it (E_s). The single ended black arrow indicates the direction of the magnetization in each case.

When linearly polarized light interacts with magnetized materials, the polarization state of the reflected light will modify in two ways. First, the polarization plane is rotated over a small angle that is characterized by Kerr rotation (θ_K), and second, the reflected light has become elliptically polarized that is called Kerr ellipticity (η_K). These modifications in the reflected light occur in the PMOKE and LMOKE. In the TMOKE, the behavior of the reflected light differs from that in the PMOKE and LMOKE. When the incident light is *s*-polarized, the *E*-field is parallel to **M**, therefore there is no interaction with the magnetic moment of the sample. When the incident light is *p*-polarized, the interaction is confined to the plane of incidence, creating an extra *E*-field component within the same plane and not generating *E*-field in perpendicular to the plane of incidence. Therefore, there are no polarization rotations in the TMOKE and magnetization M_x induces only a variation of the reflection coefficient at a non-zero incidence angle. The reflectivity of the sample depends on the magnitude and direction of the magnetization. Therefore, TMOKE can be used to measure the relative change of intensity of reflected light when a sample magnetization is revised along with positive and negative directions parallel to the sample surface.

2.2.2 Microscopic and macroscopic theory of magneto-optical effect

Phenomenologically, the optical properties in magnetic materials may be described by a dielectric function or equivalently an optical conductivity tensor in metal systems. In this section, we derive the optical conductivity from the quantum mechanical point of view. The Hamiltonian of the motion of the electron in an external field with the vector potential A and the external electromagnetic field is [61,62]

$$\widehat{H} = \frac{1}{2m}\left(\mathbf{p} + \frac{e}{c}\mathbf{A}_M + \frac{e}{c}\mathbf{A}_E\right)^2 + V(\mathbf{r}) \tag{2.11}$$

where $\mathbf{p}$ is the electron momentum operator, $\mathbf{A}_M$ is the vector potential of the applied magnetic field, and $\mathbf{A}_E$ is the vector potential of the electromagnetic wave. The Hamiltonian in Eq. (2.11) can be divided into an unperturbed H_0, the optical interaction term H_I, and the magnetic interaction term H_M. The interaction involving the optical transitions can be regarded as a small perturbation. The H_M term has two parts, namely spin-orbit and Zeeman interaction. Neglecting the $\mathbf{A}_M^2$, $\mathbf{A}_E^2$, and $\mathbf{A}_M \cdot \mathbf{A}_E$ terms, the Hamiltonian becomes

$$\widehat{H} = \widehat{H}_0 + \widehat{H}_I + \widehat{H}_M \tag{2.12}$$

where

$$\widehat{H}_0 = \frac{1}{2m}p^2 + V(\mathbf{r}), \tag{2.13}$$

$$\widehat{H}_I = \frac{e}{mc}\mathbf{A}_L \cdot \mathbf{p}. \tag{2.14}$$

$$\widehat{H}_M = \xi\mathbf{L} \cdot \mathbf{S} + \mu_B(\mathbf{L} + 2\mathbf{S}) \cdot \mathbf{B}, \tag{2.15}$$

The electron-photon interaction and the Zeeman interaction energy is very small compared to other interactions, typically 10^{-5} – 10^{-4} eV.

With electric dipole approximation, the term $\widehat{H}_I$ may express by

$$\widehat{H}_I(t) = -\mathbf{p}_e \cdot \mathbf{E}(t), \tag{2.16}$$

where $\mathbf{p}_e = e\mathbf{r}$ is the electric dipole moment of the electron. It states the interaction of energy with dipoles in an electric field and explains why the transition is called an 'electric-dipole' transition. First order time-dependent perturbation theory shows the transition between the stationary states induced by $\widehat{H}_I(t)$. The transition probability per unit time $W_{\mathbf{k}}$ by absorbing a photon of energy $\hbar\omega$ at given $\mathbf{k}$ point in the Brillouin zone is obtained from Fermi's Golden rules:

$$W_{\alpha\beta} = \frac{2\pi}{\hbar}\int \left|\langle j'|\widehat{H}_I|j\rangle\right|^2 \frac{2}{8\pi^3}\delta\big(E_{j'}(\mathbf{k}) - E_j(\mathbf{k}) - \hbar\omega\big)d^3k\,, \tag{2.17}$$

where $\left|\langle j'|\widehat{H}_I|j\rangle\right|$ is the dipole matrix element, $|j\rangle$ and $|j'\rangle$ are the occupied initial and unoccupied final states of the transition, respectively, and delta function $\delta\left(E_{j'}(\mathbf{k}) - E_j(\mathbf{k}) - \hbar\omega\right)$ expresses energy conservation with E_j and $E_{j'}$ are the energies of the initial and final states, respectively. The transition probability is proportional to the square of the dipole matrix element.

The transition probability per unit volume multiplied by the energy of the photon is the power loss function. This power loss can be expressed in terms of the optical conductivity, thus creating the link between microscopic theory and macroscopic phenomena. The power absorbed by a solid of volume *V* interacting with an electric field *E* is given by [63]

$$P = \frac{1}{2}\int Re(\mathbf{J}^* \cdot \mathbf{E})\, dV = \frac{1}{2} Re\left(\sum_{ij} \sigma_{ij} E_j^* E_i\right). \tag{2.18}$$

The optical conductivity tensor, $\sigma_{\alpha\beta}$, can be separated into two terms: the interband and intraband contributions. For the interband contribution, the optical conductivity tensor with magnetization **M** was calculated by applying the Kubo formula in the linear response theory, [64,65]

$$\sigma_{\alpha\beta}(\omega, \mathbf{M}) = \frac{ie^2}{m^2\hbar V}\sum_{\mathbf{k}}\sum_{jj'} \frac{1}{\omega_{jj',\mathbf{k}}}\left(\frac{\prod^{\alpha}_{j'j,\mathbf{k}}\prod^{\beta}_{jj',\mathbf{k}}}{\omega - \omega_{jj',\mathbf{k}} + i/\tau} + \frac{\left(\prod^{\alpha}_{j'j,\mathbf{k}}\prod^{\beta}_{jj',\mathbf{k}}\right)^*}{\omega + \omega_{jj',\boldsymbol{k}} + i/\tau}\right), \tag{2.19}$$

where *V* is a volume of a unit cell, ω is photon energy, and $\hbar\omega_{jj',\mathbf{k}}$ is an energy difference between an unoccupied state j' and an occupied state j at **k,** $\varepsilon_{j',\mathbf{k}} - \varepsilon_{j,\mathbf{k}}$. The momentum matrix elements $\Pi^{\alpha}_{j'j,\mathbf{k}} = \langle j', \mathbf{k}|p_\alpha|j, \mathbf{k}\rangle$, where $p_\alpha = -i\hbar\nabla_\alpha$ and α is the Cartesian components (*x*, *y*, and *z*), are constructed by using Bloch states $|j, \mathbf{k}\rangle$s obtained by FLAPW calculations. The quantity τ is the relaxation time parameter, where several previous calculations were used the 1/τ values from 0.1 to 0.7 eV for transition metal systems such as Fe [64,65], Cu [66], Co/Cu [65], and Co/Pt [67]. The optical matrix elements are calculated with the converged results within a self-consistent loop. Then, the optical conductivities are obtained by adding all possible optical matrix elements. Equation (2.18) clearly states the relationship between the macroscopic optical conductivity tensor and microscopic optical transitions.

In this thesis, we will restrict ourselves to the cases of the PMOKE and TMOKE

geometries with sample magnetizations of M_z and M_x, respectively. For the PMOKE geometry with M_z, the optical conductivity tensor is composed by diagonal and the off-diagonal components in the form

$$\sigma_{\alpha\beta} = \begin{pmatrix} \sigma_{xx} & \sigma_{xy} & 0 \\ \sigma_{yx} & \sigma_{yy} & 0 \\ 0 & 0 & \sigma_{zz} \end{pmatrix}, \tag{2.20}$$

where $\sigma_{xx} = \sigma_{yy}$ and $\sigma_{yx} = -\sigma_{xy}$. For the TMOKE geometry with M_x, the optical conductivity tensor is of the form

$$\sigma_{\alpha\beta} = \begin{pmatrix} \sigma_{xx} & 0 & 0 \\ 0 & \sigma_{yy} & \sigma_{yz} \\ 0 & \sigma_{zy} & \sigma_{zz} \end{pmatrix}, \tag{2.21}$$

where $\sigma_{zy} = -\sigma_{yz}$. The elements of $\sigma_{\alpha\beta}$ are complex numbers and are represented by $\sigma_{1\alpha\beta} + i\sigma_{2\alpha\beta}$ throughout the present paper.

In addition, the selection rules for electric dipole transitions must be satisfied, i.e., [68]

$$\Delta l = \pm 1, \tag{2.22a}$$
$$\Delta m_l = 0, \pm 1. \tag{2.22b}$$

These are rules about the quantum numbers of the initial and final states. The first selection rule indicates that only transitions between *s* and *p* orbitals, or *p* and *d* orbitals are allowed. In the second rule, the transitions with $\Delta m_l = +1$ and $\Delta m_l = -1$ correspond to left and right circularly polarized light (LCP and RCP), respectively. Since $\Pi^{\pm} = \Pi^x \pm i\Pi^y$ corresponds to the optical matrix for LCP and RCP, the off-diagonal component, σ_{2xy}, in the PMOKE geometry shows the MO absorption, which is proportional to the difference in the LCP and RCP between an occupied initial state *j* and an unoccupied final state *j'*. This shows that the σ_{2xy} is non-zero if contributions of the LCP and RCP transitions are different. The σ_{1xx} is an optical absorption measuring the corresponding average in the LCP and RCP transitions, which satisfies the selection rule of $\Delta m_z = \pm 1$ (for in-plane electric field polarization $E \perp c_z$), while the σ_{1zz} is an optical absorption that satisfies $\Delta m_z = 0$ (for out-of-plane electric field polarization $E \parallel c_z$). On contrary, as for M_x in the TMOKE geometry, since the quantum axis is along *x*-axis, the optical transitions with $\Delta m_x = +1$ and $\Delta m_x = -1$ for the LCP and RCP transitions may be adopted by $\Pi^{\pm} = \Pi^y \pm i\Pi^z$.

Next, we consider the modification of the electronic structure by the "magnetic" Hamiltonian. It is known that the spin-orbit (SO) interaction and exchange interaction is the most important perturbations lifting the degeneration of electronic states, which in turn is responsible for the MOKE. [46] The SO Hamiltonian, $\widehat{H}_{SO} = \xi \mathbf{L} \cdot \mathbf{S}$, is an interaction between the atomic orbital momentum **L** and the atomic spin momentum **S**, where ξ is the spin-orbit coupling strength. The SO interaction energy in terms of the potential function *V*(r) and the quantum number *l*, *s*, and *j*, which *j* = *l* + *s*, is

$$\Delta E = \frac{\hbar}{4m^2c^2}[j(j+1) - l(l+1) - s(s+1)]\frac{1}{r}\frac{dV(r)}{dr}. \tag{2.23}$$

The Hamiltonian of Heisenberg exchange between the resulting spin of two neighboring atoms may be given by:

$$\widehat{H}_{ex} = \sum_{ij} J_{ij}\mathbf{S}_i \cdot \boldsymbol{S_j}. \tag{2.24}$$

where J_{ij} being the exchange integral of the *i*th and *j*th ions. It is important to note that the exchange field affects only the spin of the ion, and in this sense, it is not equivalent to a magnetic field.

Let's try to figure out how the exchange and SO interactions induce energy level splitting. Figure 2.3 explains the optical transition from occupied states to unoccupied states, inspired by [69]. The left-hand side represents the majority (↑) states, and the right-hand side is the minority (↓) states. In the notation $|lm\rangle$, *l* is the orbital quantum number (*l* = 1 for *p* states and *l* = 2 for *d* states), and *m* is the magnetic quantum number that takes integer values in the interval (–*l*, *l*). Assuming a ferromagnetic material is magnetized along the *z*-direction, the exchange interaction splits the energy level of the electronic states, where the majority spin states have smaller energy than the minority spin states. We ignore the exchange splitting in *p* levels. The SO interaction lifts the energy level degeneracy of *m* for both *p* or *d* states. Noting that for the majority spins, the energy increases with *m*, although the situation is reversed for the minority spins.

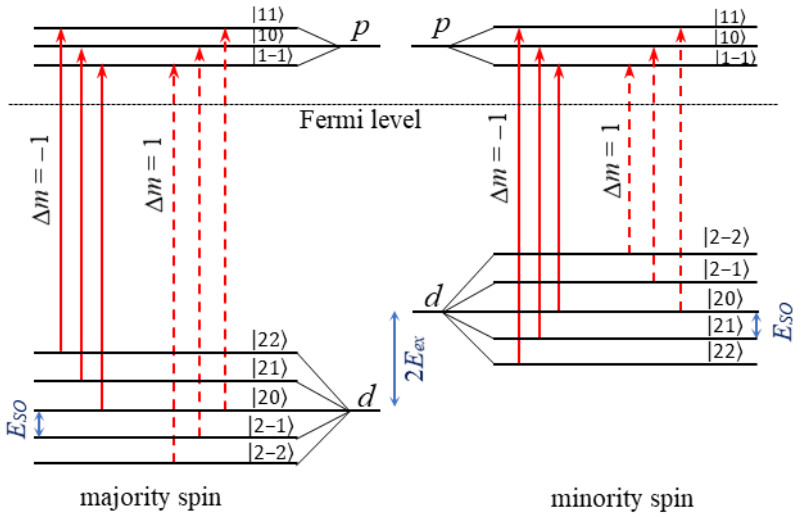

Figure 2.3: Schematic modification of the electronic structure of *p* and *d* state with exchange and SO interactions energy. The arrows indicate the allowed electric dipole transitions, with the solid and dotted lines represent RCP and LCP corresponding to $\Delta m = -1$ and $\Delta m = 1$, respectively.

MO effects result from magnetically induced off-diagonal component in the optical conductivity tensor or dielectric function. In general, a possible source for non-vanishing σ_{2xy} is dominant from the lifting of the degeneracy of energy level. [65] This source is from the SO and exchange interaction, as mentioned earlier. As an example, let us consider a transition between a doubly degenerate $d_{xy,yz}$ level ($l = 2$, $m_l = \pm 1$) and p_z level ($l = 1$, $m_l = 0$). If there is no SO interaction, the dipole matrix elements for LCP and RCP are the same, as shown in Fig. 2.4a. Therefore, the off-diagonal component of the conductivity is canceled out for each total spin state, but the diagonal component, which is the sum of LCP and RCP, remains without spin-orbit interaction. If there is no exchange interaction, there is no splitting between majority and minority spin states, as shown in Fig. 2.4b. Then, the off-diagonal component for the majority and minority spin states exactly the same, and the sum of the contributions from the two states cancels.

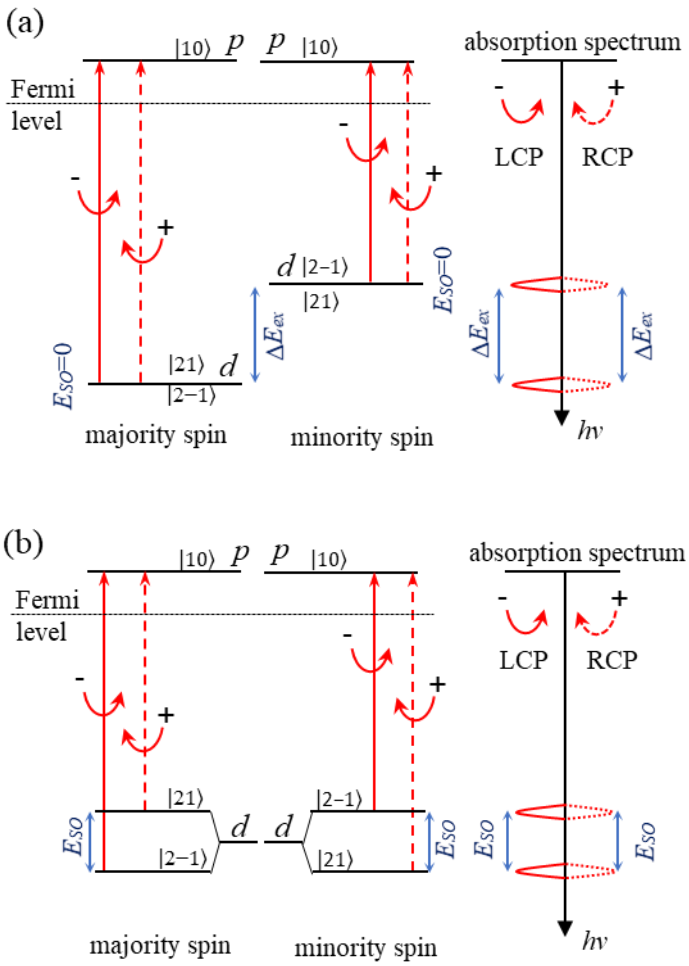

Figure 2.4: Sketch of the energy level of the electric dipole transition for LCP and RCP in the case: (a) no SO interaction and (b) no exchange interaction. The right side in (a) and (b) show the corresponding absorption spectra versus photon energy *hv*.

In addition to the interband contribution, there is the intraband contribution which correspond to the electronic conduction by free carrier. Drude model has been used for the intraband contribution,

$$\sigma_D(\omega) = \frac{\omega_p^2}{4\pi(\gamma_D - i\omega)}, \tag{2.25}$$

where γ_D is the relaxation time Drude parameter and is usually known from experiments. The plasma frequency ω_p, directly related to the momentum operator, has been deduced from our DFT calculations. However, the contribution of the intraband transition to the off-diagonal conductivity is usually not considered.

The dielectric function $\varepsilon_{\alpha\beta}$ is related to the optical conductivity tensor $\sigma_{\alpha\beta}$ through

$$\varepsilon_{\alpha\beta}(\omega) = \delta_{\alpha\beta} + \frac{i4\pi}{\omega}\sigma_{\alpha\beta}(\omega), \tag{2.25}$$

where $\delta_{\alpha\beta}$ is Kronecker delta, and ω is photon energy. Optical observables like complex refractive index, $\tilde{n}(\omega) = n(\omega) + i\kappa(\omega)$, can be obtained from the dielectric function through

$$\tilde{n}_{\alpha\alpha}(\omega) = \sqrt{\varepsilon_{\alpha\alpha}(\omega)}. \tag{2.26}$$

Here, we are setting the relative magnetic permeabilities are approximated to one at optical frequency, $\mu_r(\omega) = 1$. [65]

We review the MO observable in MOKE configuration. In the polar geometry, the expression for the complex Kerr angle is given by [64]

$$\Phi_K = \phi_K + i\epsilon_K = \frac{-\sigma_{xy}}{\sigma_{xx}\sqrt{1 + i\left(\frac{4\pi}{\omega}\right)\sigma_{xx}}}. \tag{2.26}$$

Here ϕ_K is the real Kerr rotation angle, and ϵ_K is the Kerr ellipticity. In the transverse geometry, the magnitude of TMOKE signal ($\Delta R/R$) as differences in the reflectivity at opposite directions of the magnetization is defined as [33]

$$\frac{\Delta R}{R} = \frac{R_{pp}(+M) - R_{pp}(-M)}{R_{pp}(+M) + R_{pp}(-M)} \tag{2.27}$$

where $R_{pp}(+M)$ and $R_{pp}(-M)$ are the reflectivity of the *p*-polarised light for positive and negative magnetization, respectively. Subindice *pp* emphasize that polarization conversion (the presence of *ps* or *sp* terms) does not occur in TMOKE configuration. The maximum reachable value of $\Delta R/R$ is 1.

2.3 Light propagations in a multilayer system

2.3.1 4×4 transfer matrix methods

In order to calculate the MO effect of the multilayers system, Zak et al. [60] developed a universal approach based on the medium boundary *A* and the medium propagation *D* matrices. We consider an arbitrary direction of the magnetization **M** with respect to the plane incidence *yz* and the plane of separation *xy* shown in Fig. 2.5. In the TMOKE configuration, the **M** direction is in polar angles $\varphi = \pi/2$ and $\gamma = 0$. The dielectric function of a magnetic medium having an arbitrary direction of **M** can be generalized as follows:

$$\varepsilon = \varepsilon_{xx}\begin{pmatrix} 1 & i\cos\varphi\, Q & -i\sin\gamma\sin\varphi\, Q \\ -i\cos\varphi\, Q & 1 & i\cos\gamma\sin\varphi\, Q \\ i\sin\gamma\sin\varphi\, Q & -i\cos\gamma\sin\varphi\, Q & 1 \end{pmatrix} \tag{2.28}$$

where Q is the magneto-optical constant. We assume $\varepsilon_{xx} = \varepsilon_{yy} = \varepsilon_{zz}$ for simplicity.

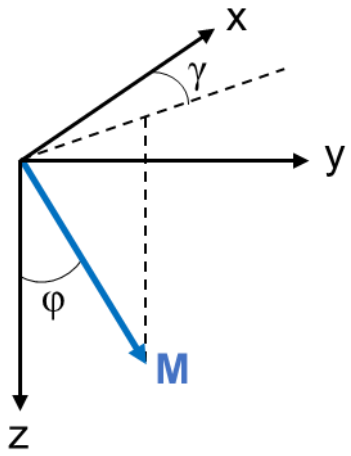

Figure 2.5: Spherical coordinates for the magnetization **M** in the *xyz* system. *M* is the magnetization. γ and φ is the angle of **M** with the *x* and *z* direction, respectively.

We assume that the *xy* plane represents the separation plane between two media. The medium boundary *A* connects the two following vectors *F* and *P*:

$$F = AP, \tag{2.29}$$

where *F* vector contains the *x* and *y* components of the electric **E** and magnetic **H** fields, and *P* vector contains the components of **E** on the *p* and *s* direction. Then, two column vector *F* and *P* is denoted by:

$$F = \begin{bmatrix} E_x \\ E_y \\ H_x \\ H_y \end{bmatrix}, P = \begin{bmatrix} E_s^i \\ E_p^i \\ E_s^r \\ E_p^r \end{bmatrix}, \tag{2.30}$$

where *i* and *r* denote the incident and reflected light, and *s* and *p* denote the perpendicular and the parallel direction to the plane of incident light, respectively. The medium boundary matrix *A* having arbitrary direction of **M** can be expressed by

$$A = \begin{bmatrix} 1 & 0 & 1 & 0 \\ \frac{i}{2}\frac{\alpha_y}{\alpha_z}QB & \alpha_z + i\alpha_y \sin\varphi \cos\gamma\, Q & \frac{i}{2}\frac{\alpha_y}{\alpha_z}QC & -\alpha_z + i\alpha_y \sin\varphi \cos\gamma\, Q \\ \frac{i}{2}Ng_iQ & -N & \frac{iN}{2\alpha_z}g_rQ & -N \\ N\alpha_z & \frac{iN}{2\alpha_z}g_iQ & -N\alpha_z & -\frac{iN}{2\alpha_z}g_rQ \end{bmatrix}, \quad (2.31)$$

where

$$\alpha_y = \sin\theta\,, \quad (2.32a)$$
$$\alpha_z = \cos\theta\,, \quad (2.32b)$$
$$B = \alpha_y g_i - 2\sin\varphi \sin\varphi\,, \quad (2.32c)$$
$$C = \alpha_y g_r - 2\sin\varphi \sin\varphi\,, \quad (2.32d)$$
$$g_i = \cos\varphi\, \alpha_z + \alpha_y \sin\varphi \sin\gamma\,, \quad (2.32e)$$
$$g_r = -\cos\varphi\, \alpha_z + \alpha_y \sin\varphi \sin\gamma\,. \quad (2.32f)$$

Here N is the refractive index of medium and θ is the complex refractive angle determined by Snell's law.

The medium propagation matrix takes into account the change in the phase of the wave when the wave propagates through the medium of thickness d, expressed by

$$D = \begin{bmatrix} U & U\delta_i & 0 & 0 \\ -U\delta_i & U & 0 & 0 \\ 0 & 0 & U^{-1} & -U^{-1}\delta_r \\ 0 & 0 & U^{-1}\delta_r & U^{-1} \end{bmatrix}, \quad (2.33)$$

where

$$U = \exp\left(-i\frac{2\pi}{\lambda}Nd\alpha_z\right), \quad (2.34a)$$
$$\delta_i = \frac{\pi}{\lambda\alpha_z}NdQg_i, \quad (2.34b)$$
$$\delta_r = \frac{\pi}{\lambda\alpha_z}NdQg_r. \quad (2.34c)$$

We consider the multilayer system as shown in Fig. 2.6. The beam light passes from the initial medium i, goes through the multilayer system, and ends up in the final medium f. The condition in this process is given by the so-called 4×4 M matrix,

$$M = A_i^{-1}\prod_{m=1}^{l}(A_m D_m A_m^{-1})\, A_f, \quad (2.35)$$

where l is the total number of layers in the system, A_i and A_f are the medium boundary matrices for initial and final media, and A_m and D_m are the medium boundary and the

propagation matrices, respectively, for the *m*-th layer. The 4×4 *M* matrix can be expressed in the form of 2×2 block matrices as follows:

$$M = \begin{bmatrix} G & H \\ I & J \end{bmatrix} \tag{2.36}$$

The magneto-optical Fresnel reflection coefficients can be given as

$$\begin{bmatrix} r_{ss} & r_{sp} \\ r_{ps} & r_{pp} \end{bmatrix} = IG^{-1}, \tag{2.37}$$

where *r* is the reflection coefficient. The subscript in each coefficient identifies the perpendicular (*s*) or parallel (*p*) component of the electric field with respect to the reflection plane.

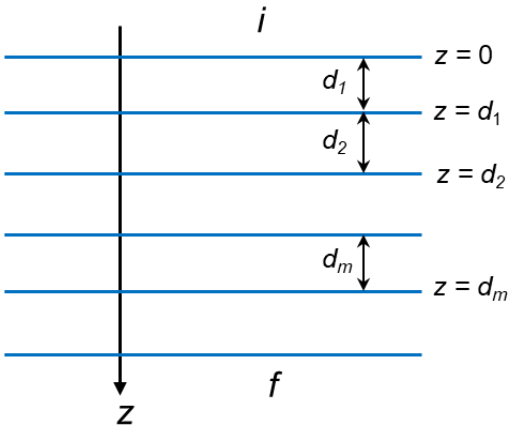

Figure 2.6: Multilayer system. *d* is the thickness of the layer. *i* and *f* label the initial and final media. *m* is the running index of the layers.

2.3.2 Reflectivity of three-layer system

We consider the three-layer system at the transverse magnetization, which consists of non-magnetic medium 0, magnetic medium 1, and non-magnetic medium 2. The medium boundary matrix *A* for non-magnetic and magnetic medium can be expressed by

$$A_{0,2} = \begin{bmatrix} 1 & 0 & 1 & 0 \\ 0 & \alpha_{z0,2} & 0 & -\alpha_{z0,2} \\ 0 & -N_{0,2} & 0 & -N_{0,2} \\ N_{0,2}\alpha_{z0,2} & 0 & -N_{0,2}\alpha_{z0,2} & 0 \end{bmatrix}, \tag{2.38}$$

and

$$A_1 = \begin{bmatrix} 1 & 0 & 1 & 0 \\ 0 & \alpha_{z1} + i\alpha_{y1}Q_1 & 0 & -\alpha_{z1} + i\alpha_{y1}Q_1 \\ 0 & -N_1 & 0 & -N_1 \\ N_1\alpha_{z1} & 0 & -N_1\alpha_{z1} & 0 \end{bmatrix}, \tag{2.39}$$

respectively. For propagation through a layer a thickness d_1, we find the propagation matrix D_1

$$D_1 = \begin{bmatrix} U_1 & 0 & 0 & 0 \\ 0 & U_1 & 0 & 0 \\ 0 & 0 & U_1^{-1} & 0 \\ 0 & 0 & 0 & U_1^{-1} \end{bmatrix}. \tag{2.40}$$

The matrix product M can be written as

$$M = A_0^{-1}A_1D_1A_1^{-1}A_2. \tag{2.41}$$

Here, A_0, A_1, and A_2 are the boundary matrix of medium 0, medium 1, and medium 2, respectively. The reflection coefficients for p-polarized can be expressed by

$$r_{pp} = \frac{M_{42}}{M_{22}} = \frac{WU_1^2 + X}{YU_1^2 + Z}, \tag{2.42}$$

where

$$W = -\frac{N_2\alpha_{y1}^2}{N_1\alpha_{z2}\alpha_{z1}}Q_1^2 - \left(\frac{N_2\alpha_{z0}}{N_0\alpha_{z2}} + 1\right)\frac{a_{y1}}{\alpha_{z1}}iQ_1 - \frac{N_2}{\alpha_{z2}}\left(\frac{\alpha_{z0}}{N_0} + \frac{\alpha_{z1}}{N_1}\right) + \frac{N_1\alpha_{z0}}{N_0\alpha_{z1}} - 1, \tag{2.43a}$$

$$X = \frac{N_2\alpha_{y1}^2}{N_1\alpha_{z2}\alpha_{z1}}Q_1^2 - \left(\frac{N_2\alpha_{z0}}{N_0\alpha_{z2}} - 1\right)\frac{a_{y1}}{\alpha_{z1}}iQ_1 - \frac{N_2}{\alpha_{z2}}\left(\frac{\alpha_{z0}}{N_0} - \frac{\alpha_{z1}}{N_1}\right) - \frac{N_1\alpha_{z0}}{N_0\alpha_{z1}} - 1, \tag{2.43b}$$

$$Y = \frac{N_2\alpha_{y1}^2}{N_1\alpha_{z2}\alpha_{z1}}Q_1^2 - \left(\frac{N_2\alpha_{z0}}{N_0\alpha_{z2}} - 1\right)\frac{a_{y1}}{\alpha_{z1}}iQ_1 - \frac{N_2}{\alpha_{z2}}\left(\frac{\alpha_{z0}}{N_0} - \frac{\alpha_{z1}}{N_1}\right) + \frac{N_1\alpha_{z0}}{N_0\alpha_{z1}} + 1, \tag{2.43c}$$

$$Z = -\frac{N_2\alpha_{y1}^2}{N_1\alpha_{z2}\alpha_{z1}}Q_1^2 - \left(\frac{N_2\alpha_{z0}}{N_0\alpha_{z2}} + 1\right)\frac{a_{y1}}{\alpha_{z1}}iQ_1 - \frac{N_2}{\alpha_{z2}}\left(\frac{\alpha_{z0}}{N_0} - \frac{\alpha_{z1}}{N_1}\right) - \frac{N_1\alpha_{z0}}{N_0\alpha_{z1}} + 1. \tag{2.43d}$$

The intensity of reflected *p* polarized light, R_{pp}, is calculated by

$$R_{pp} = \left|r_{pp}\right|^2, \tag{2.44}$$

where r_{pp} is given by Eq. (2.42).

Chapter 3

Optical properties of 3*d*, 4*d*, and 5*d* transition metals

3.1 Introduction

Transition metals (TMs), especially noble metals, are plasmonic materials because they have large plasma frequencies and high electrical conductivity. Several studies, including optical conductivity, dielectric function, or optical constant in the TMs, have been conducted to explore the plasmonic performance. For instance, Johnson and Christy report their experimental values of the optical constants for copper, silver, and gold in the spectral range 0.5-6.5 eV and conclude that the interband absorption dominates in the visible and ultraviolet regimes. [70] On the theoretical counterparts, Uba et al. apply the GGA approximation with Hubbard energy correction to improve the description of the optical conductivity spectra of noble metal. [66] The dielectric function of metal ε_m has an important role in SPR. It is well known that the dielectric function of a good plasmonic metal must fulfill two properties, namely, the real part must be negative, $\mathrm{Re}\varepsilon_m < 0$, and the imaginary part are small enough, $\mathrm{Im}\varepsilon_m \ll -\mathrm{Re}\varepsilon_m$.

In this chapter, in order to provide a systematic analysis on the SPR related optical properties for the late series of transition metals, we present the results of the optical conductivities and dielectric functions of 3*d* (Fe, Ni, Co, Cu), 4*d* (Ru, Rh, Pd, Ag) and 5*d* (Os, Ir, Pt, Au) metals by using DFT calculations. [71] Next, by using the computed values, the reflectivity of the SPR curve on the three-layer system in the Kretschmann configuration is presented.

3.2 Computational methods

Self-consistent DFT, implemented in the full-potential linearized augmented plane wave (FLAPW) method. [54] were performed where the generalized gradient approximation (GGA) was used for the exchange-correlation potential. [72] The electronic wave function is expanded on a plane-wave basis set by a kinetic energy cutoff of 3.9 a.u.$^{-1}$ and angular momentum $l_{\max} = 8$ inside the muffin-tin spheres. The number of *k*-points in the first full Brillouin zone was set to 70×70×70. Crystal structures and lattice

constants of all systems were adopted from experimental structures available in Ref. [73], since in metals, the optical spectrum is relatively insensitive to small changes in the lattice parameters. [74]

The modelling was carrier out by using a three-layer systems in the Kretschmann configuration, commonly used in experiments for exciting SPP waves, as shown in Fig. 3.1. The first layer in this configuration is a prism with a dielectric function ε_p, the second layer is a transition metal with a dielectric function ε_m and thickness d, and the third layer is air as dielectric with dielectric function ε_a. The reflectivity of the system was calculated through Eq. (2.44).

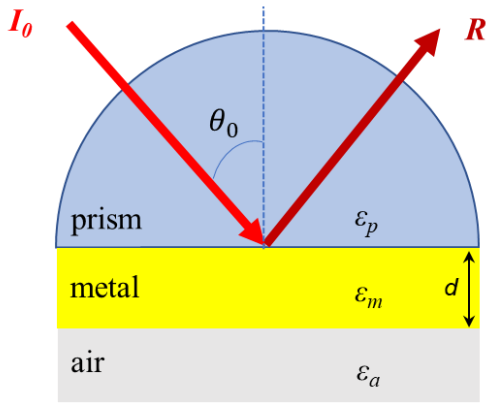

Figure 3.1: Schematic illustration of SPR configuration in the Kretschmann prism coupling system.

A N-BK7 (SCHOTT) glass was used as the prism substrate for all configurations. The dielectric function of prism ε_p and air ε_a as function of energy are obtained from Ref. [75] The complex dielectric function of the transition metal $\varepsilon_m = \varepsilon_{1xx} + i\varepsilon_{2xx}$ is taken from present calculation results. The optimum thickness of the metal layer and the incident angle are chosen so that the reflectivity has a minimum dip, shown in Table 3.1. The incident light is varied from 0 to 6 eV in the optical region (1.65-3.26 eV).

Table 3.1: The optimum thickness and incident angle used in the simulation.

	Fe	Co	Ni	Cu	Ru	Rh	Pd	Ag	Os	Ir	Pt	Au
Thickness (nm)	70	40	50	25	20	10	20	35	25	25	10	30
Incident angle (°)	50	50	50	44	50	50	50	44	50	50	50	44

3.3 Optical properties

3.3.1 Optical conductivity

We start by discussing the optical conductivities, σ_{1xx}, which include the interband and intraband contributions. Figure 3.1 shows the diagonal part of optical conductivity compared to the experimental data. It is visible that the general features of the calculated optical conductivities reproduce reasonably well to the experiments. Peaks in the spectrum of the absorptive parts of the optical conductivity σ_{1xx} have also been obtained in our calculations, resembling those measured in experiments.

In the 3*d* metals, our calculation results have the same trend and only slightly differ in amplitude, especially for Fe and Co. The peak of the experimental spectrum of Fe is located at 2-3 eV, while our calculation nicely obtained the peak at around 3 eV. In the Cu, the contribution of the Drude model is very dominant at low energy levels. However, the position of the calculated edge of the optical conductivity are shifted toward smaller energies as compared to the experimental data. This edge position shift can be confirmed from the partial σ_{1xx} spectra for the transitions from the uppermost *d* states (band 5) into s,p-like states (band 6) just above the Fermi level, especially in *X* and *L* symmetry points. Similar situations have also been found for Ag and Au from the 4*d* and 5*d* metals, respectively. The salient features of the calculated results at 1.7, 2.9 and 1.8 eV for Cu, Ag, and Au, respectively, is observed. In noble metals, intraband contributions have a significant effect on low energy, which indicates that an optimized Drude model might be crucial. [76] In other atoms, namely Ru, Rh, Pd, Os, Ir, and Pt, our results are also similar to experimental data.

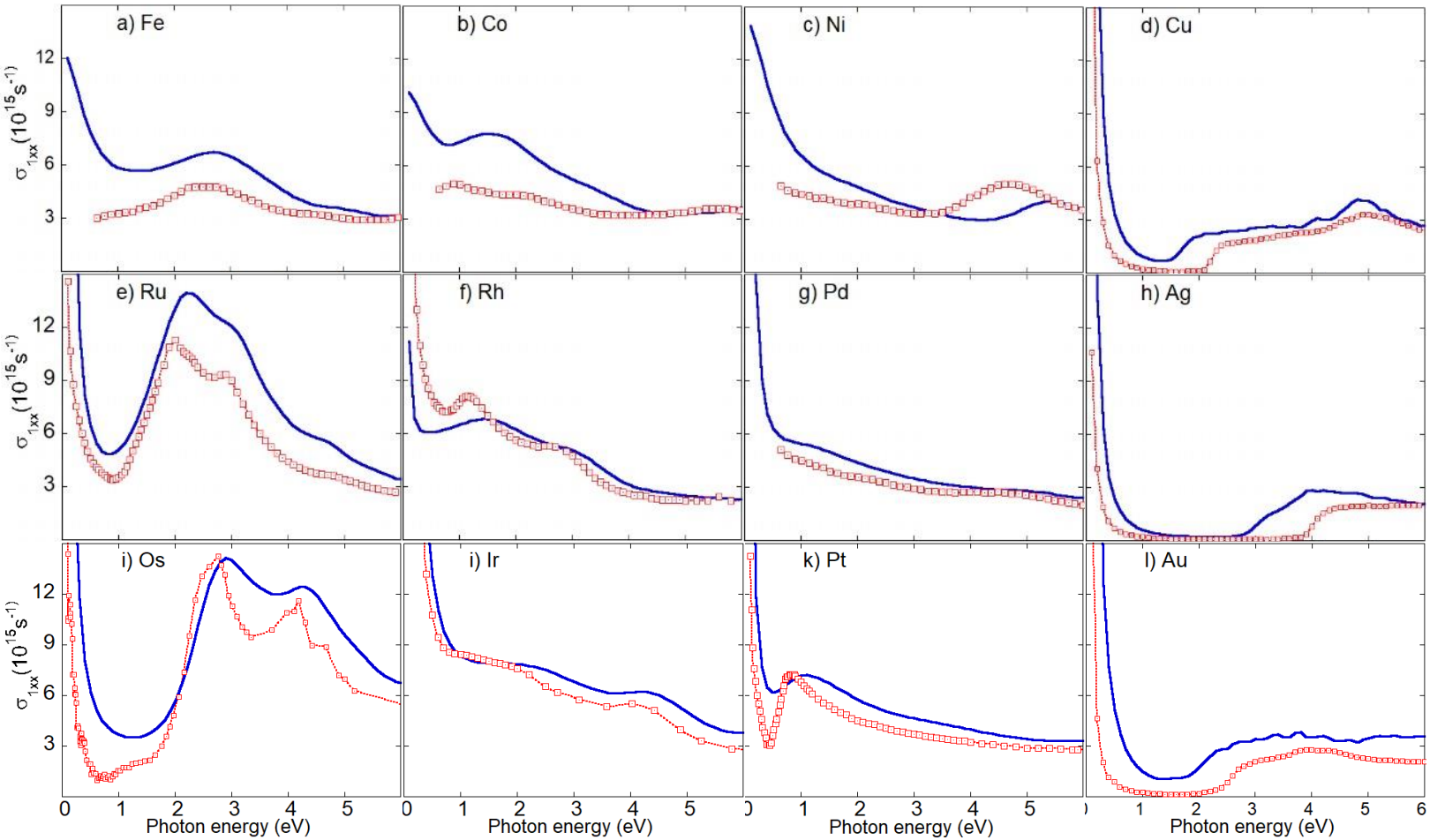

Figure 3.2: Calculated diagonal optical conductivity (blue solid lines) for transition metals atom. Dashed lines drawn by red squares are experimental data collected from literature; Fe, Co, Ni and Pd [77], Cu, Ag, and Au [78], Ru [79], Rh [80], Os [81], Ir [82], and Pt [83].

3.3.2 Dielectric functions

Calculated of the real part of dielectric functions ε_{1xx} of 3*d*, 4*d* and 5*d* TMs are shown in Fig. 3.3. Almost all calculations of ε_{1xx} are in good agreement with the experiment data. We get the zero crossings of ε_{1xx}, which represents bulk plasmon energy. Zero crossings of ε_{1xx} in Cu at low energy are not observed. In Ag, the zero crossings of ε_{1xx} first shift to lower energy at 3 eV, then at more than 4 eV, several bulk plasmon values appear. In Au, there are multiple zero-crossings of ε_{1xx} between 3.5-4.4 eV. The presence of a bulk plasmon in the optical range would facilitate the excitation of surface plasmons in these materials. Most of the transition metals in Fig. 3.3 have a negative ε_{1xx} in the optical range so that they are potential as a plasmonic material.

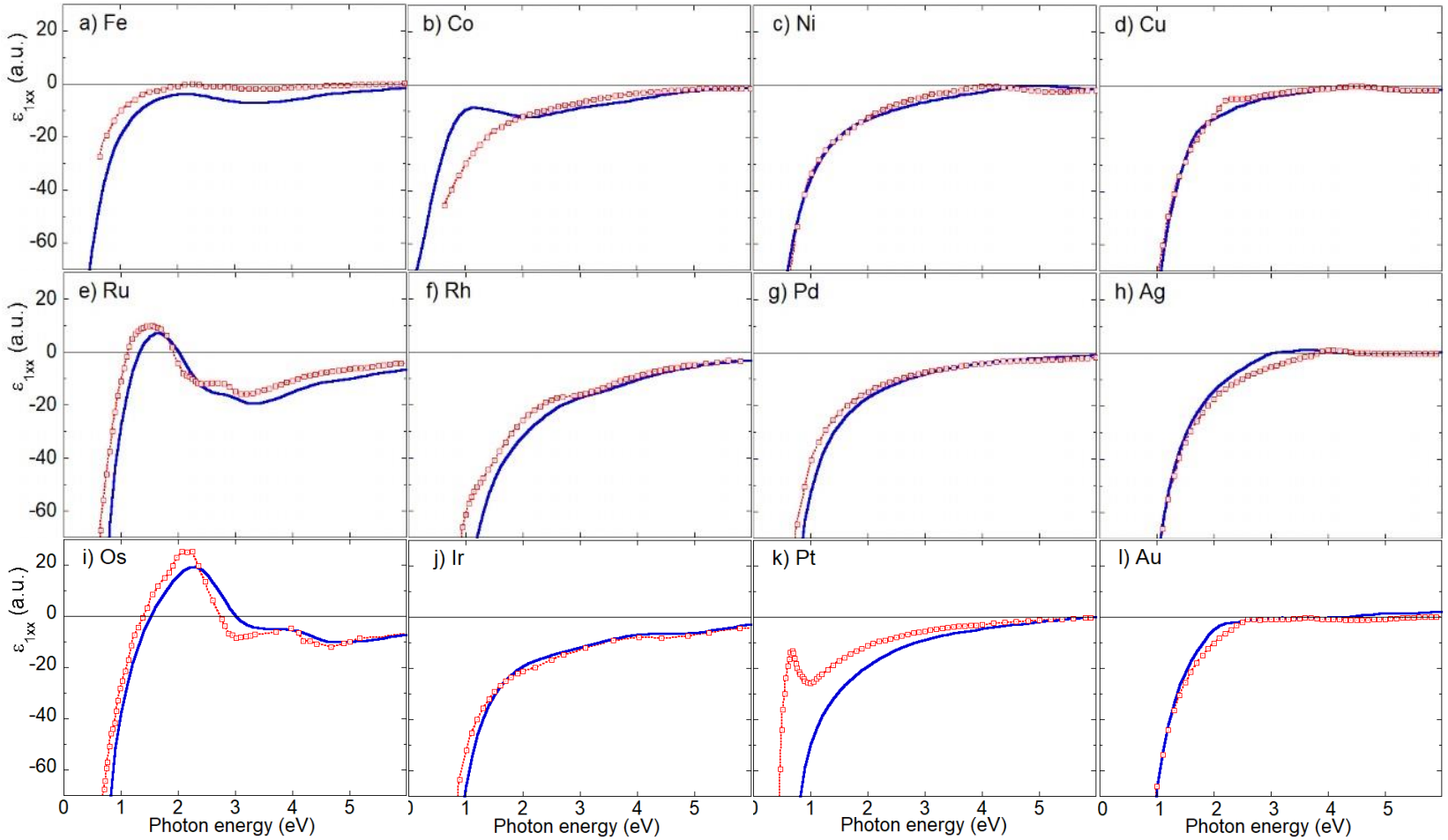

Figure 3.3: Comparison of the real part of dielectric functions for transition metals atom. Notations are the same as Figure 3.2.

The calculatied of the imaginary part ε_{2xx} are shown in Fig. 3.4. At low energy, our calculation results confirm that only noble metals have $\varepsilon_{2xx} \approx 0$. Metallic high reflectivity was observed at 1-1.5 eV, 1-3 eV, and 1-2 eV, respectively, for Cu, Ag, and Au. Compared to other atoms, Ru and Os also have dips in the low energy range so that the peak of spectra ε_{2xx} can be observed. The spectrum of ε_{2xx} has the same characteristics as that of σ_{1xx} which both represent a loss mechanism in material. Energy absorption of incident photons occurs in the interband transition process when electrons move from energy below the Fermi level to the next higher empty energy level.

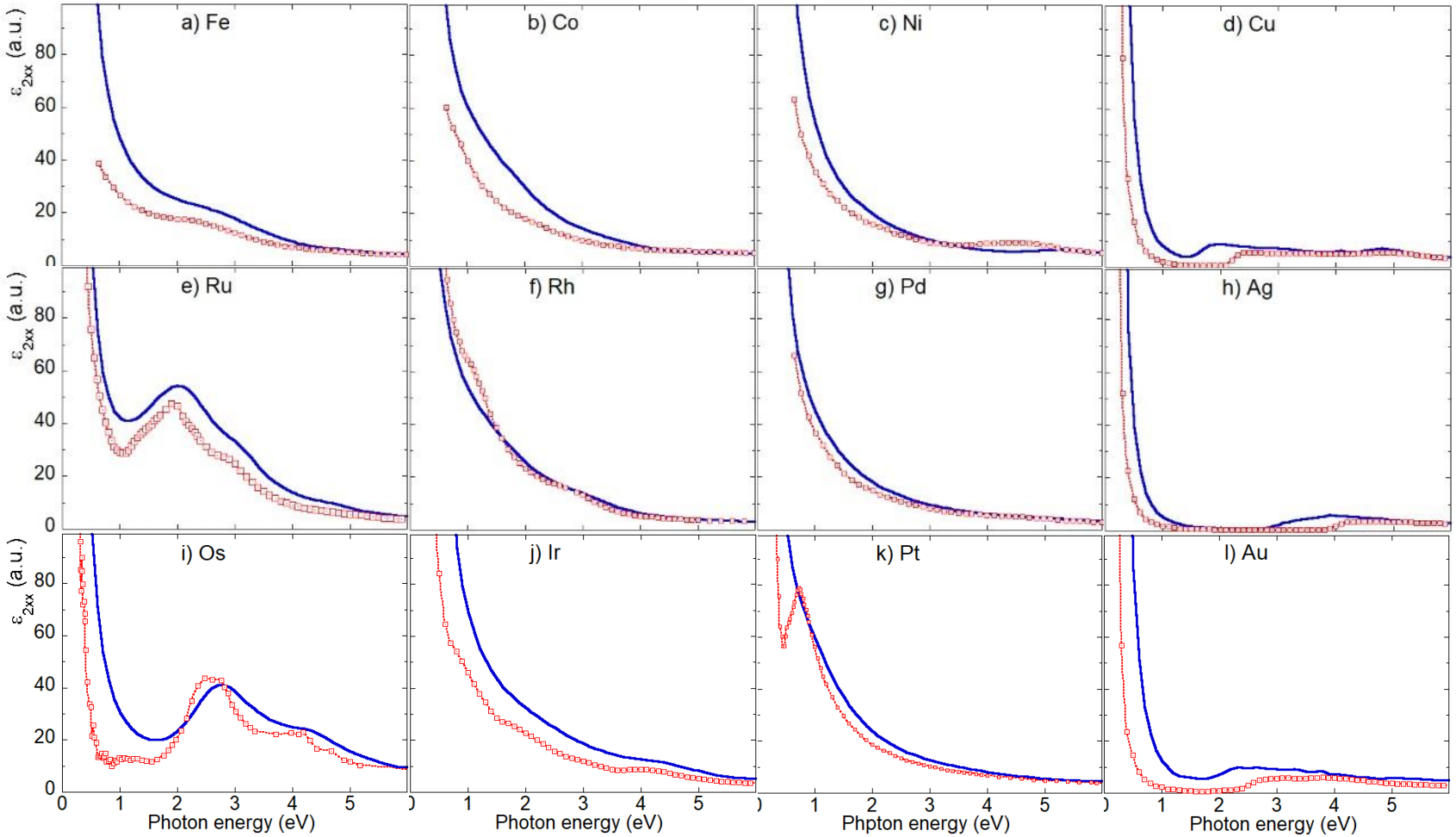

Figure 3.4: Comparison of the imaginary part of dielectric functions for transition metals atom. Notations are the same as Figure 3.2.

3.4 Reflectivity curve

To find out the material characteristics in the SPR application, we calculated the reflectivity based on Eq. (2), as shown in Figure 3.5. In the optical region, the curves that have dips are Cu, Ag, Au, Os, and Ru. We can show that noble metal (i.e., Cu, Au, and Ag) has the optimum dip with a small full-width-half-maximum (FWHM). Ru and Os also have dipped, but the FWHM is wide. The dip shows the resonance condition between the SPP wave and the evanescent wave. The imaginary part of ε_{2xx} plays an important role in determining the magnitude of the FWHM. The small ε_{2xx} will give a narrow FWHM resulting in a sharp dip.

Our simulation curve is similar to the reference in thin layers using the Kretschmann configuration. For Cu, the reflectivity calculation shifts to the left, indicating the difference in thickness of Cu used, which is 25 nm and 43.5 nm for our calculations and Ref. [84], respectively. In Ag and Au, the curve also shifts to lower energy than the reference curve caused by differences in the prism material used, namely a UV fused quartz and a CaF_2 glass for Ref. [85] and Ref. [86], respectively. The difference in prism material indicates a different refractive index, which is sensitive to reflectivity in the system.

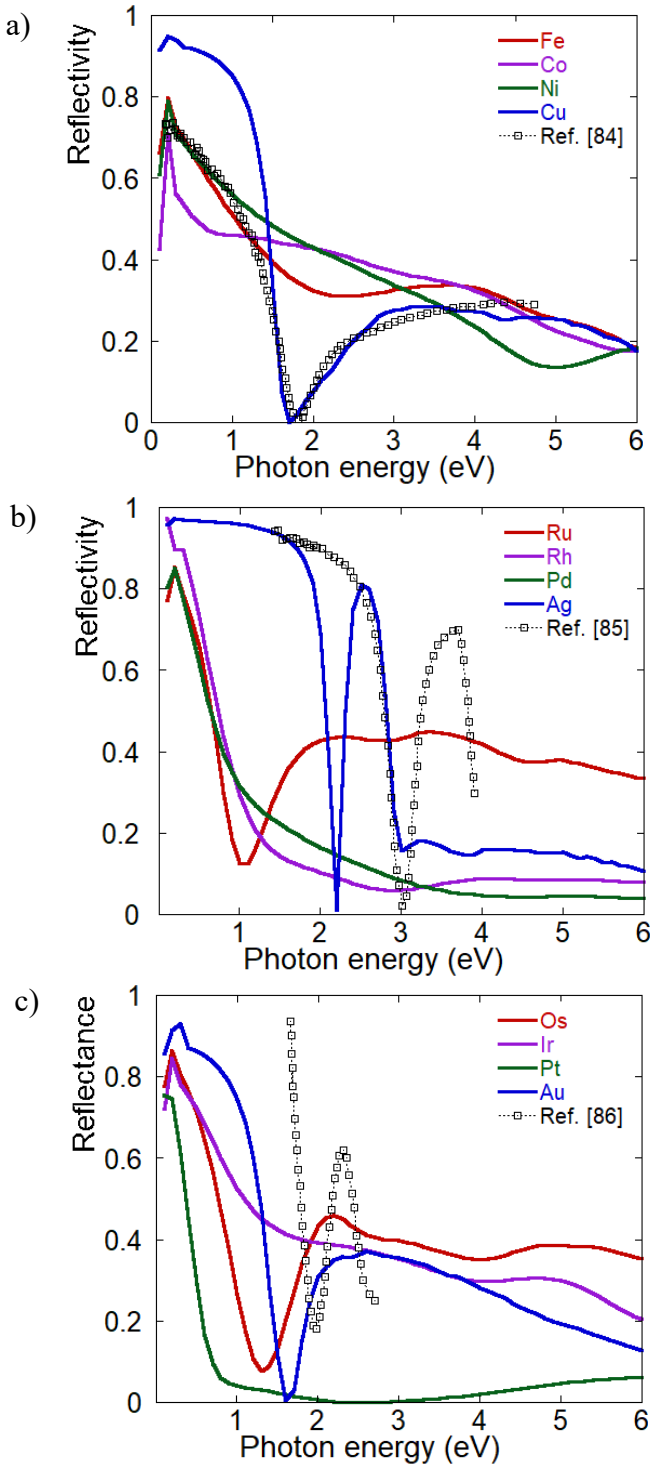

Figure 3.5: SPR reflectivity curve as a function of the energy. Lines drawn by black squares are experimental data from literature; Cu [84], Ag [85], and Au [86].

3.5 Summary

Using the first-principles calculations, we systematically calculated the optical conductivity and dielectric functions for 3*d* (Fe, Ni, Co, Cu), 4*d* (Ru, Rh, Pd, Ag), and 5*d* (Os, Ir, Pt, Au) transition metals. We obtained a good agreement with experimental data. In Fe, the peak of optical conductivity around 3 eV is reproduced by our calculation, while in the Cu, the edge position shift can be confirmed from the partial σ_{1xx} spectra. The calculated SPR reflectivity curve in the Kretschmann configuration shows a sharp dip for noble metals corresponding to a small enough of the imaginary part of the dielectric function.

Chapter 4

Optical and magneto-optical properties of the FeCu superlattices

4.1 Introduction

In 3*d* transition metals, Fe and Cu each have interesting properties. As a ferromagnetic material, Fe is easy to magnetize and offers large MO properties. Cu is the low-cost plasmonic metal possessing tunable plasmonic resonance in the visible region. The combination of Fe and Cu, which are ferromagnetic/noble metals, is particularly interesting in both multilayer and superlattice (SL) forms. [87–92] Multilayers with small repetition periods, where each layer consists of only a few atomic layers, can be easily modeled theoretically. The FeCu SL may open a vesta for magnetoplasmonic applications in MOSPR. The special interest in the FeCu SL arises from the fact that the small lattice mismatch between fcc Fe and Cu of 0.83% [93] and high Curie temperature of 400 K [87] . However, one of the main physical parameters in magnetoplasmonic is the optical losses in the structure. These optical losses are caused by the interband transition, which consists of optical absorption and MO absorption.

This chapter reports on the first-principles study to explain the origin of optical and magneto-optical properties of FeCu SL. In the first stage, we present the electronic properties, such as density of states and band structure, then discuss the feature of optical conductivity and dielectric function of FeCu SLs. Based on the band-by-band decomposition analysis, we discuss the electronic origin of optical and MO anisotropies in the Fe_1Cu_1 SL. [94].

4.2 Computational methods

Models of the Fe_xCu_x SLs with x = 1, 2, and 3 atomic-layers were constructed by atomic-layer stackings with a body-centered alignment along (001) direction, schematically presented in Fig. 4.1. The case with x = 1 corresponds to an ordered Fe_1Cu_1 SL in the $L1_0$ type. Both in-plane and out-of-plane lattice constants, a and c, were fully optimized based on a total energy minimization.

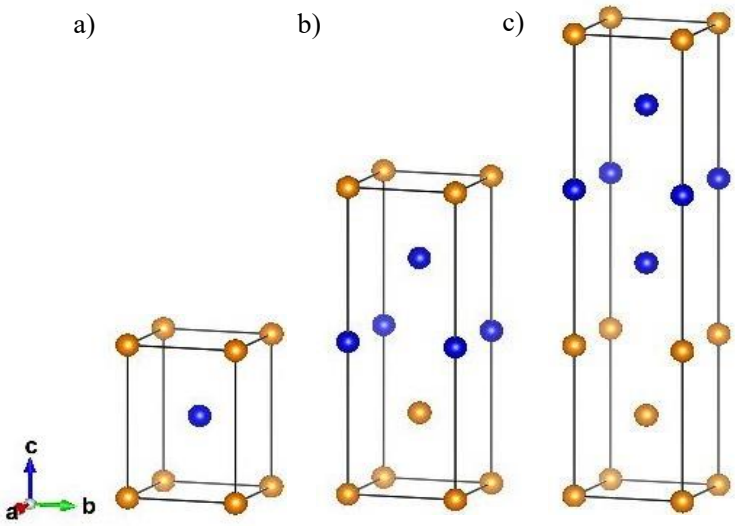

Figure 4.1: The unit cells used for Fe_1Cu_1, Fe_2Cu_2, and Fe_3Cu_3 SLs. Brown spheres are Cu atoms and blue ones are Fe atoms.

Electronic structure of the Fe_xCu_x SLs were calculated by using full-potential linearized augmented plane wave (FLAPW) method based on generalized gradient approximation (GGA) of exchange-correlation potential. [54,72] The wave function was expanded by a plane-wave basis set with a cutoff of 3.9 bohr^{-1} (K_{max}) and the maximum number of angular momentums was chosen to 8 (l_{max}), and the muffin-tin radius set to 2.2 bohr (R_{MT}) for both Fe and Cu atoms, where $R_{MT}K_{max} \sim l_{max}$ was adopted. The spin-orbit coupling (SOC) was treated by using the second variational method. The sample magnetization of M_z and M_x are oriented along the out-of-plane [001] and the in-plane [100] directions, respectively. In M_x, the m-decomposed weights of orbitals may be transformed in accordance with a rotation matrix, $D^{l}_{m'm}(\theta,\phi)$. [95]. For the Brillouin zone (BZ) integration, k-point meshes of 51×51×51 were used. The relaxation time τ is assumed to $1/\tau = 0.5$ eV for the interband transitions. The Drude model has been used to combine the intraband contribution with the optical conductivity.

4.3 Structural, magnetic, and electronic properties

4.3.1 Structural and magnetic properties

The calculated of the structural properties of the Fe_xCu_x SLs are summarized in Table 4.1. The optimized in-plane lattice constants are close to the experimental results of the $[Fe_1/Cu_1]_{100}$ multilayer of 3.596 Å [96], while the c/a in Fe_1Cu_1 SLs results in 1.04, agreed with that in the previous calculation. [97] It was found that there was a decrease

in the in-plane lattice constant for x = 2 and 3 by 0.56% and 0.84%, respectively, compared to those of x = 1. Importantly, the Fe-Cu interlayer spacing in the SLs is found to increase as the x increases, while the Fe-Fe interlayer spacing at x = 2 and 3 are almost half that at x = 1, indicating that the interlayer spacing may play an important role for the electronic properties of the SLs.

Table 4.1. The calculated of in-plane and out-of-plane lattice constant, a and c, of the Fe_xCu_x SLs. The Fe-Cu and Fe-Fe distance are the atomic interplane spacing along the z direction, respectively.

Superlattices	Fe_1Cu_1	Fe_2Cu_2	Fe_3Cu_3
a (Å)	3.57	3.55	3.54
c (Å)	3.72	7.56	11.41
Fe-Cu (Å)	1.86	1.89	1.89
Fe-Fe (Å)	-	1.92	1.94

The calculated spin and orbitals magnetic moments for M_z and M_x are listed in Table 4.2 and 4.3, respectively. In the sample magnetization M_z, a large moment about 2.646 μ_B is found for Fe layer may belong to the $L1_0$ family of ferromagnets, agrees with the previous calculations of 2.67μ_B. [98] We can confirm that the magnetic moment of Fe layer in the ordered $L1_0$ of FeCu SL is between 2.2μ_B and 3.4μ_B, which is the magnetic moment for bulk bcc Fe and free-standing Fe ML, respectively. The enhancement of magnetic moment of Fe in FeCu SL can be caused by reducing the symmetry of system [99] or lattice expansion in plane of Fe sandwiched by Cu atoms [100]. The change of magnetization direction shows that the spin magnetic moment does not change while the orbitals magnetic moment changes slightly.

TABLE 4.2. The calculated spin magnetic moment M_S (in μ_B) of Cu and Fe atoms in atomic layers of Fe_xCu_x SLs with magnetization direction M_z and M_x.

	M_z			M_x		
Atom	Fe_1Cu_1	Fe_2Cu_2	Fe_3Cu_3	Fe_1Cu_1	Fe_2Cu_2	Fe_3Cu_3
Cu1	0.092	0.051	0.060	0.092	0.051	0.060
Cu2		0.049	0.008		0.049	0.008
Cu3			0.061			0.061
Fe1	2.646	2.623	2.593	2.647	2.623	2.593
Fe2		2.616	2.603		2.616	2.603
Fe3			2.596			2.596

TABLE 4.3. The calculated orbital magnetic moment M_L (in μ_B) of Cu and Fe atoms in atomic layers of Fe_xCu_x SLs with magnetization direction M_z and M_x.

	M_z			M_x		
Atom	Fe_1Cu_1	Fe_2Cu_2	Fe_3Cu_3	Fe_1Cu_1	Fe_2Cu_2	Fe_3Cu_3
Cu1	0.010	0.005	0.006	0.009	0.004	0.004
Cu2		0.004	0.001		0.004	0.000
Cu3			0.006			0.004
Fe1	0.055	0.057	0.055	0.044	0.058	0.056
Fe2		0.057	0.056		0.058	0.055
Fe3			0.055			0.056

4.3.2 Electronic properties

The calculated partial densities of states (PDOSs) of Fe and Cu atoms in Fe_xCu_x SLs with magnetization direction M_x are shown in Fig. 4.2. For the Fe_1Cu_1 (x = 1) SL, The PDOS at the vicinity of Fermi energy (E_F), at around −1.5 eV to 2 eV, consists of mainly the Fe *d* orbitals with the minority-spin state. A large exchange splitting in the Fe *d* orbitals can be seen, which leads to the large magnetic moment of 2.646 μ_B, as observed in the free-standing Fe monolayer (ML). [101] The fact that the Cu *d* orbitals are almost occupied and are located around −5 to −2 eV gives rise to a weak hybridization between the Fe *d* and Cu *d* orbitals, which induces a small exchange splitting in the Cu atoms with the moment of 0.092 μ_B. It is noted that when the number of monolayer (MLs), *x*, increase, there are a change in the peaks of PDOS in the Fe-minority states and the hybridization

between the neighboring Fe and Cu orbitals becomes stronger. The bandwidth of the hybridization in Fe minority states which located around Fermi energy are 4.0, 4.6 and 4.8 for x = 1, 2, and 3, respectively, marked with the black arrow in Figs. 4.2(a-b) and Fig. 4.3(a).

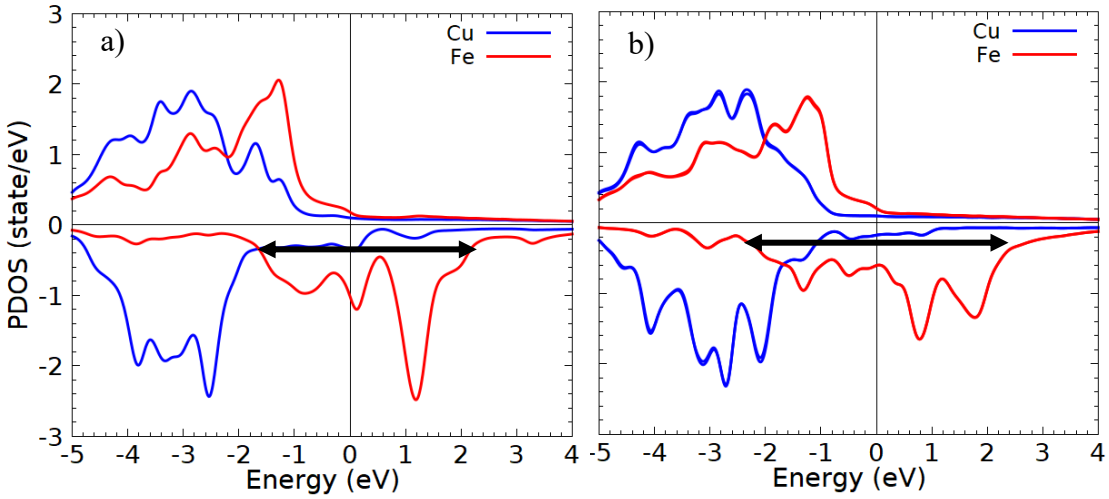

Figure 4.2: Partial density of states (PDOSs) of (a) Fe_1Cu_1 and (b) Fe_2Cu_2 SLs.

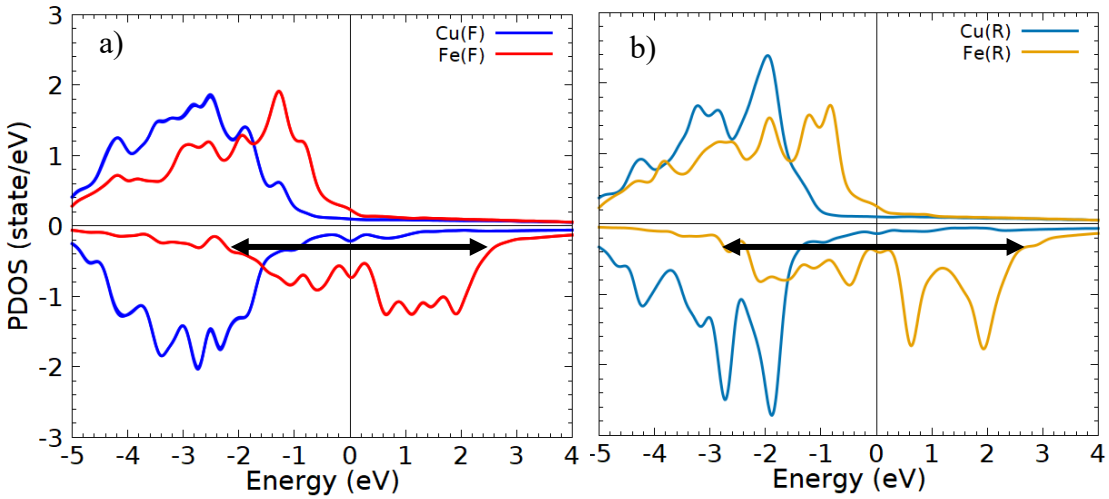

Figure 4.3: Partial density of states (PDOSs) of Fe_3Cu_3 SLs for (a) interface and (b) interior atoms.

Figures 4.4(a-b) show the band structure of the Fe_1Cu_1 SLs, where the weights of wave functions of the *d* orbitals in the Fe minority-spin states, by projecting to the quantum m_z- and m_x-numbers along z- and *x*-axes, respectively, are plotted by linewidth. The band structure with sample magnetization of M_z can be discerned as an analogy of two-dimensional feature as seen in the free-standing Fe ML [101], as shown in Fig. 4.4(a). The out-of-plane *dd* hybridization between the $d_{z^2-r^2}$ orbitals in the next nearest

neighboring Fe atoms along the plan normal can be seen in the vicinity of E_F from –0.1 to 1.0 eV. The Fe $d_{xz,yz}$ orbitals with the in-plane *dd* bonding and antibonding states are seen to cross E_F from –1.7 to 1.2 eV. It however notes that the Fe *d* orbitals weakly couple to the Cu *d* orbitals via the d_{xz} and d_{yz} orbitals due to an Fe-Cu *dd* hybridization. The Fe $d_{m_z=\pm 2}$ $(= d_{xy,x^2-y^2})$ orbitals located above and below E_F show a large dispersion along to *M*-Γ-*X*-*M* of the in-plane **k**-path, due to the strong in-plane *dd* hybridization between the neighboring in-plane Fe atoms. Importantly, the *p* orbitals at Fe and Cu atoms, which are highly dispersive, couple weakly to the *d* orbitals; p_z couples to $d_{xz,yz}$ and $p_{x,y}$ couple to d_{xy,z^2-r^2} by through *pd* hybridizations.

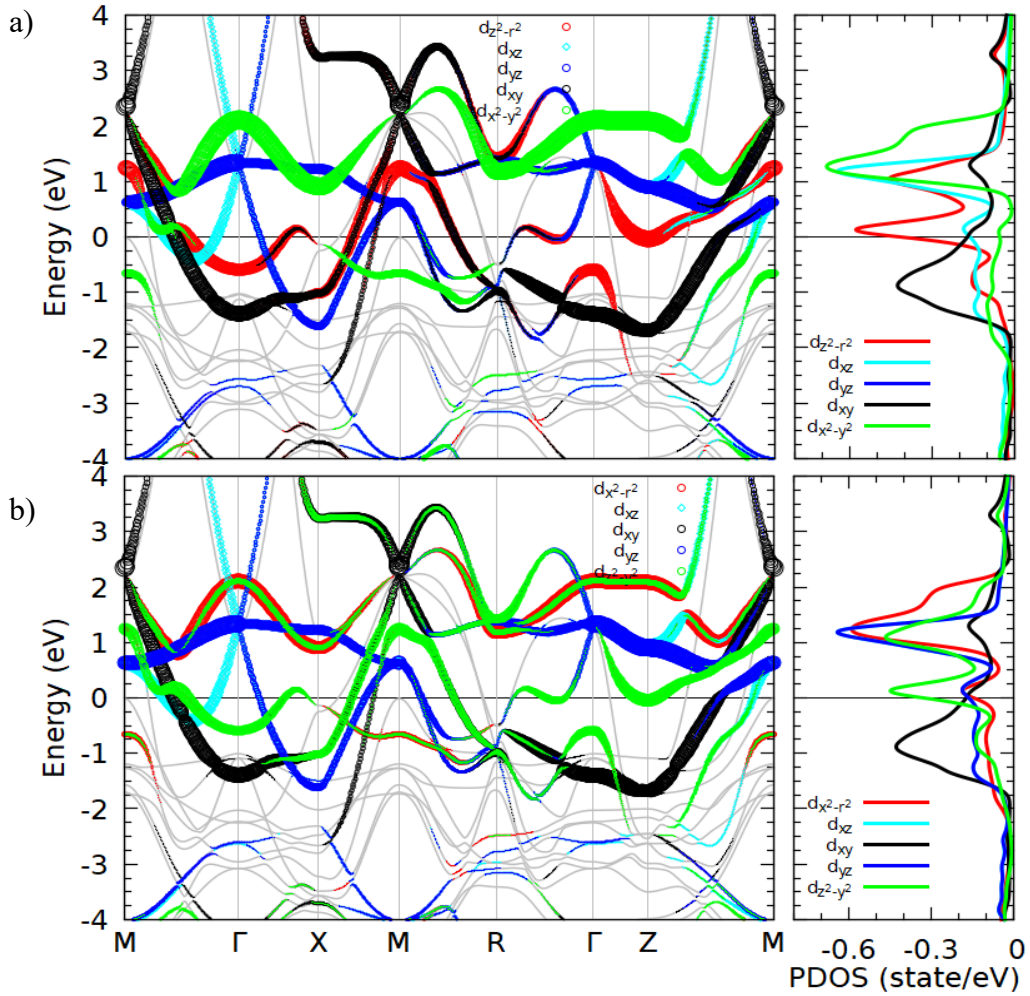

Figure 4.4: Fully relativistic band structures (left panel) and partial density of states for Fe *d* orbitals (right panel) with the minority-spin state of Fe_1Cu_1 SLs with magnetization oriented along (a) the out-of-plane, M_x, and (b) in-plane, M_x, direction. The real space projected weights of Fe *d* orbitals are marked by colors and linewidth.

Figure 4.4(b) shows the band structure when the sample magnetization orients along *x*-axis, M_x, where eigenvalues in the whole **k**-space do not vary much compared to those for M_z due to the small SOC strength in Fe and Cu atoms. Due to the transformation corresponds to the rotation matrix, the weight of the $d_{m_z=\pm2}$ ($= d_{xy,x^2-y^2}$) orbitals along *M*-Γ-*X* transforms into a linear combination of those of $d_{m_x=\pm1}$ ($= d_{xy,xz}$) and $d_{m_x=0}$ ($= d_{x^2-r^2}$) orbitals. It notes that the flat band of $d_{xz,yz}$ ($d_{x^2-r^2}$) orbitals around Γ (*R* and Γ) points form the peaks of DOS at an unoccupied states around 1.2 (1.2 and 2.0) eV. The electronic properties of Fe_2Cu_2 and Fe_3Cu_3 SLs for Fe minority-spin state with sample magnetization of M_x are described in the next paragraph.

In the Fe_2Cu_2 SLs, two MLs of Fe significantly changes the electronic properties of an unoccupied states, as shown in Fig. 4.5. The reduction of the Fe-Fe interlayer spacing, which is almost half that of Fe_1Cu_1 SLs, causes the Fe *dd* hybridization via d_{xz,yz,z^2-y^2} orbitals to be more intensive. As a result, the flat band of $d_{xz,yz}$ ($d_{z^2-y^2}$) orbitals around Γ point splits into two regions at 0.6 (-1.4) and 1.8 (0.4) eV. Meanwhile, the contraction of the in-plane lattice constant causes the shift of the flat band of $d_{x^2-r^2}$ orbitals around *R* point which approaches E_F at 0.9 eV. The contraction also makes the bandwidth of in-plane Fe *dd* hybridization via d_{xy} orbitals wider than in Fe_1Cu_1 SLs from -2.0 to 2.4 eV.

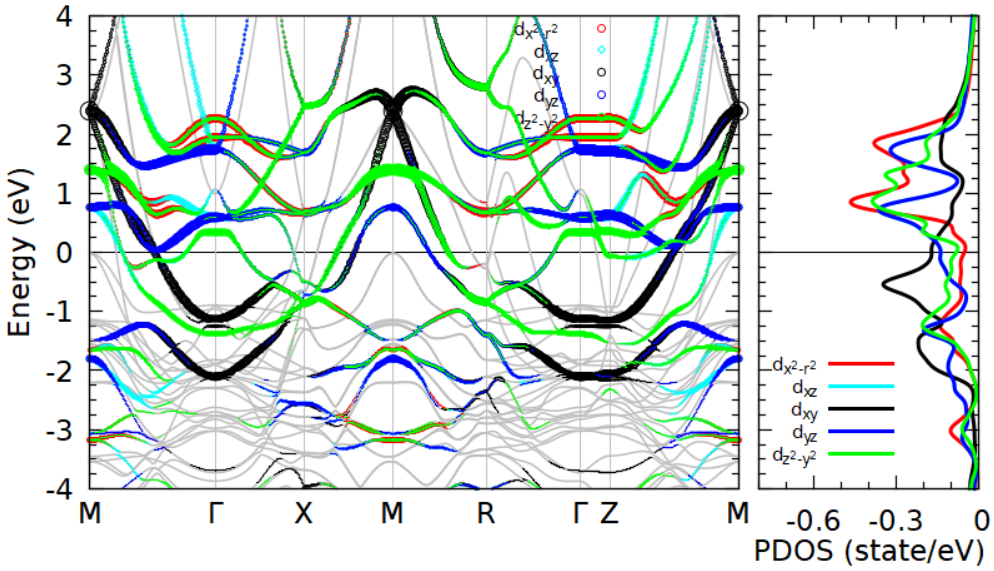

Figure 4.5: Fully relativistic band structures (left panel) and partial density of states for Fe *d* orbitals (right panel) with the minority-spin state of Fe_2Cu_2 SLs. Notations are the same as Fig. 4.4

When the number of MLs increases in the Fe_3Cu_3SLs, the bands attributed in Fe atoms at the interface and interior layers, which are denoted by Fe(F) and Fe(R), respectively, behave different characteristics, as shown in Figs. 4.6(a) and 4.6(b). In the Fe(F), the $d_{xz,yz}$ orbitals represent delocalized orbitals between 0.0 and 2 eV above the E_F with the flat band at the Γ point located at 0.4, 1.3, and 2.0 eV, as shown in Fig. 4.6(a). The DOS peak of $d_{z^2-y^2}$ orbitals in Fe(F) of about 1.0 eV replace the two peaks in Fe(R) due to the out-of-plane Fe *dd* hybridization between the neighboring out-of-plane Fe atoms. Meanwhile, in the Fe(R) the flat band of $d_{xz,yz}$ orbitals at Γ point around 0.5 and 2.0 eV form DOS peaks at minority states which are both farther apart than in Fe_2Cu_2 SLs, as shown in Fig. 4.6(b). The bandwidth of in-plane Fe *dd* hybridization via d_{xy} orbitals from -2.2 eV to 2.4 eV was also found to widen due to the contraction of the in-plane lattice constant. Therefore, tuning electronic properties in the vicinity of E_F in SLs can be done through bandwidth, i.e., degree of hybridization, by changing the number of MLs.

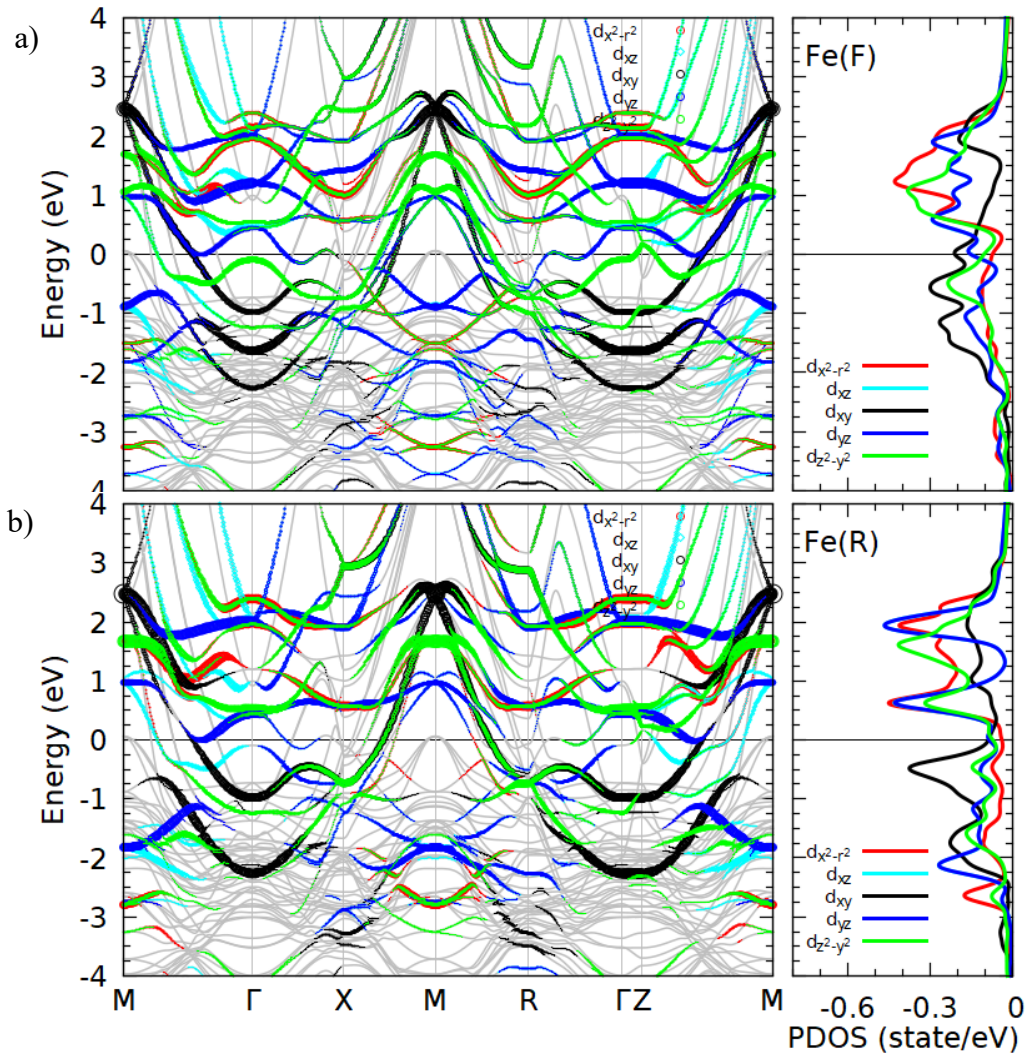

Figure 4.6: Fully relativistic band structures (left panel) and partial density of states for Fe *d* orbitals (right panel) with the minority-spin state of of Fe_3Cu_3 SLs for (a) Fe(F) and (b) Fe(R). Notations are the same as Fig. 4.4

4.4 Optical conductivity and dielectric function

4.4.1 Optical conductivity

The interband contribution of the diagonal component of the optical conductivities of the Fe_xCu_x SLs with in-plane (001) magnetization is summarized in Fig. 4.7. The prominent peak of the real part of the diagonal component, σ_{1xx}, at around 1.5, 2.4 and 2.0 eV for x = 1, 2, and 3, respectively, dominated by the interband transition of Fe atoms, as shown in Fig. 4.7(a), while the imaginary parts, σ_{2xx}, are negative in low photon energy ω and increase as ω increases, as shown in Fig. 4.7(b). A sign change in σ_{2xx} shifts to lower ω as x increases.

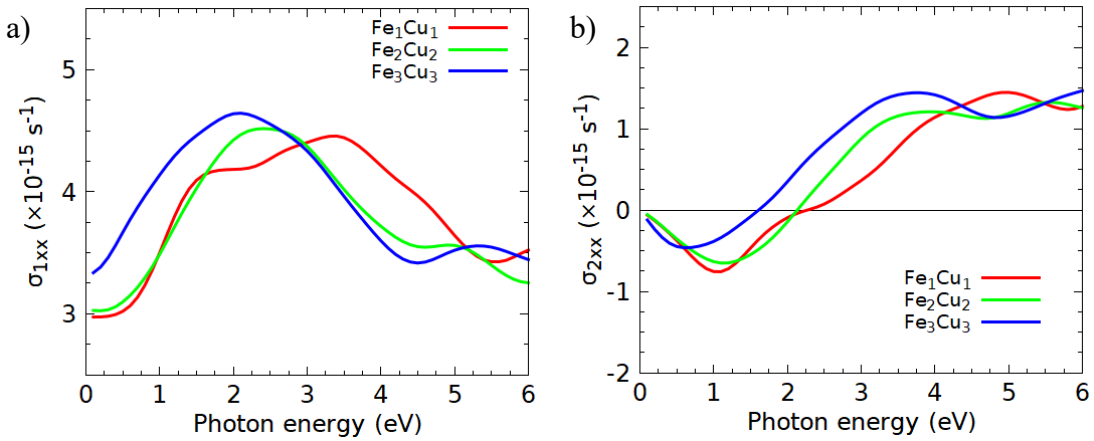

Figure 4.7: The interband contribution of the diagonal component of the optical conductivity: (a) and (b) are the real and imaginary parts, σ_{1xx} and σ_{2xx}, respectively.

The calculation of the contribution of each atomic layer to the interband transition shows that the peak spectra of σ_{1xx} in the Fe_xCu_x SLs are dominated by Fe atom, as shown in Figs. 4.8(a-c). The gray vertical lines and blue arrows indicate the peak position of the σ_{1xx} in the Fe_xCu_x SLs and Fe atom, respectively. In the Fe_1Cu_1 SLs, the contribution along the *M*–Γ–*X*–*M*–*R*–Γ–*Z*–*M* path to the interband transitions of Fe atom at 1.5 eV is shown in Fig. 4.8(d), which correspond to the in-plane Fe-Fe and out-of-plane FeCu *dd* hybridization along Γ–*X*–*M* and *M*–*R*–Γ path, respectively. It shows that the hybridization process plays an important role in the interband transition. [102]

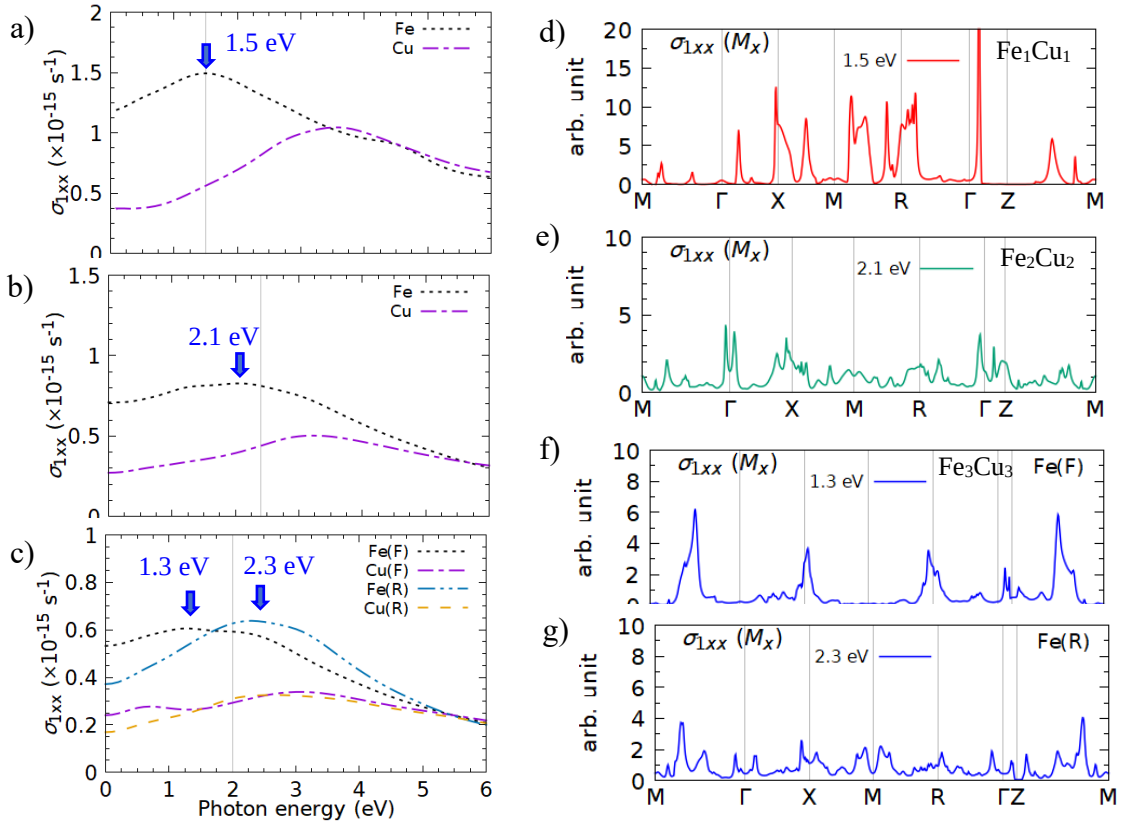

Figure 4.8: Contribution of individual Fe and Cu atoms to the σ_{1xx} spectra (left panel) and *k*-path of σ_{1xx} spectra from Fe atom (right panel) of Fe_xCu_x SLs.

In the Fe_2Cu_2 SLs, a blueshift of the peak spectra from 1.5 eV to 2.4 eV is found. The shift is dominated by the peak interband transition of Fe atom around 2.1 eV. The increasing contribution around Γ (X) point to the interband transitions at 2.1 eV due to the influence of the out-of-plane (in-plane) Fe dd hybridization via $d_{z^2-y^2}$ ($d_{x^2-r^2}$) orbitals, as shown in Fig. 4.8(e). The redshift of peak in Fe_3Cu_3 SLs is a superposition of the interband transition contributions of Fe(F) and Fe(R), which have peaks around 1.3 and 2.3 eV, respectively. In the Fe(F) atoms, the contribution around Γ, M, X, and R points to interband transitions at 1.3 eV mainly from *p* to *d* orbitals due to the Fe *dd* hybridization via d_{yz} orbitals, as shown in Fig. 4.8(f). In the Fe(R) atoms, the contribution to interband transitions at 2.3 eV is evenly distributed along the *k*-path of all *d* orbitals, as shown in Fig. 4.8(g). It is found that the energy band having high DOS at high symmetry point usually dominates the interband transition, e.g., interband transition via $d_{x^2-r^2}$ orbitals located 0.5 (2.0) eV above E_F contributes small peaks around *X* (*R*) point. The increasing the number of MLs on SLs can shift the flat energy band at a high symmetry point due to the hybridization process so that it can tune the interband transition.

In the off-diagonal components of the optical conductivity with in-plane (001) magnetization, the real parts, σ_{1yz}, decrease as w increases, while the imaginary parts, σ_{2yz}, exhibit the prominent peaks located around 1.7, 1.9, and 1.4 eV for x =1, 2, and 3, respectively, as shown in Figs. 4.9(a) and 4.9(b). The physical interpretation of σ_{2yz} is magneto-optical absorption which proportional to the difference in absorption rate of the left and right circularly polarized (LCP and RCP) lights. In the low energy, the positive value of σ_{2yz} suggests that interband transitions related to LCP light should be stronger. The nonvanishing of σ_{2yz} is a spin orbit-coupling effect in the form of the lifting of energy level degeneracies, hybrid mixing different spin characters, and spin-flip transitions. [65] Hence, we calculated the σ_{2yz} spectra by switching off the SOC strength at Fe(Cu) atom artificially. As a result, the Fe SOC plays a role in demonstrating these spectra, as shown in the Fig. 4.10 for Fe_1Cu_1 SLs. It is found that, for example, a mixed state of d_{yz} and $d_{z^2-y^2}$ character is located at 1.2 eV above E_F along the *M*-*R* path; see Fig. 4.4(b).

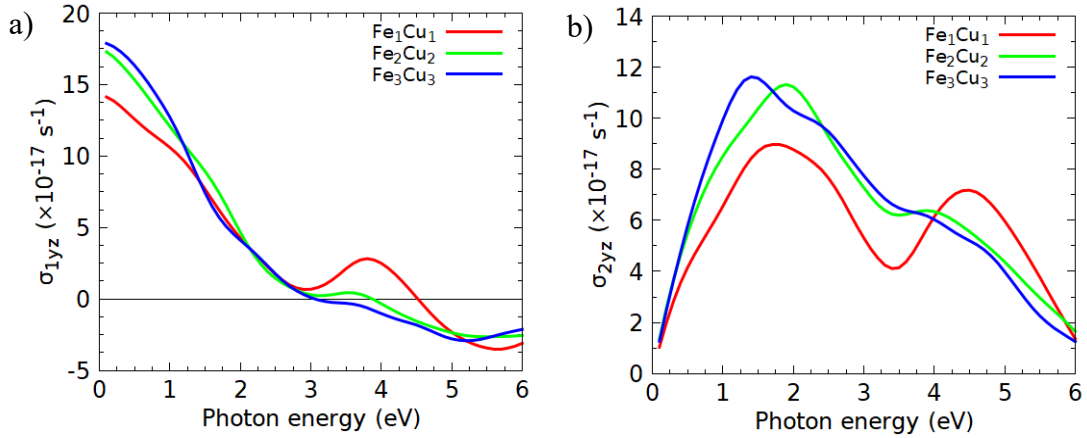

Figure 4.9: The interband contribution of the off-diagonal component of the optical conductivity: (a) and (b) are the real and imaginary parts, σ_{2yz} and σ_{2yz}, respectively.

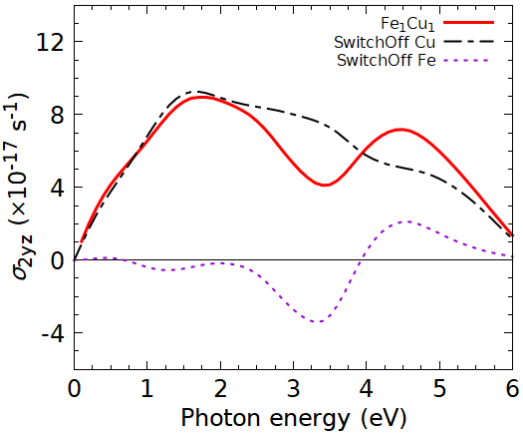

Figure 4.10: Contribution of the SO coupling set to zero on Cu site (dot-dash black lines) and Fe site (dot purple lines) to the σ_{2yz} spectra of Fe_1Cu_1 SLs.

4.4.2 Dielectric function

The dielectric functions $\varepsilon_{\alpha\beta}$ is related to the optical conductivity tensor $\sigma_{\alpha\beta}$ through Eq. (2.25). The diagonal components of the dielectric functions are presented in Figs. 4.11(a-b), which reflect the contribution of both interband and intraband transitions into the optical spectrum. The negative value of ε_{1xx} indicates that Fe_xCu_x SLs is metallic with a high plasma frequency (> 6 eV), and the positive value of ε_{2xx} is slightly lower than that of bulk Fe. Therefore Fe_xCu_x SLs can be applied as plasmonic materials in the optical range although they have higher optical losses than pure noble metals. The trend of prominent peaks of ε_{2xx} follows σ_{1xx} spectrum through Eq. (2.25). In the optical range, tuning the optical properties can be done by a varying number of MLs of SLs.

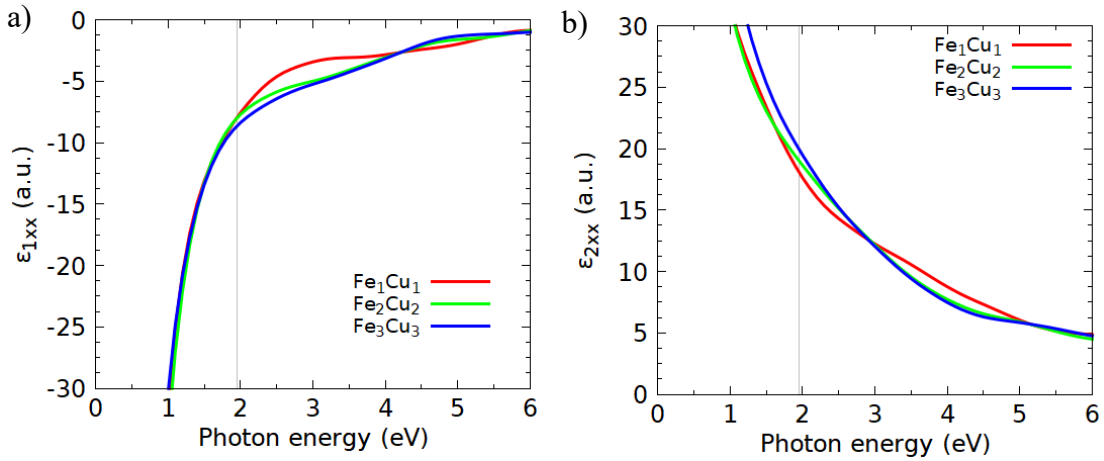

Figure. 4.11: (a) and (b) show the real and imaginary parts of the diagonal component ε_{xx} dielectric functions of Fe_xCu_x SLs, respectively. The gray vertical lines indicate the HeNe laser energy at 1.96 eV.

In the off-diagonal component, as shown in Figs. 4.12(a-b), the absolute value of ε_{1yz} of the Fe_2Cu_2 and Fe_3Cu_3 SLs is almost the same but it is more significant than the Fe_1Cu_1 SLs. The small valley of about 2.0 and 1.4 eV for the Fe_2Cu_2 and Fe_3Cu_3 SLs, respectively, correspond to blue shift and redshift in the peaks of σ_{2xy} spectra. The non-vanishing of the off-diagonal component shows that FeCu SLs offer a MO effect, which has the potential as a magnetoplasmonic structure.

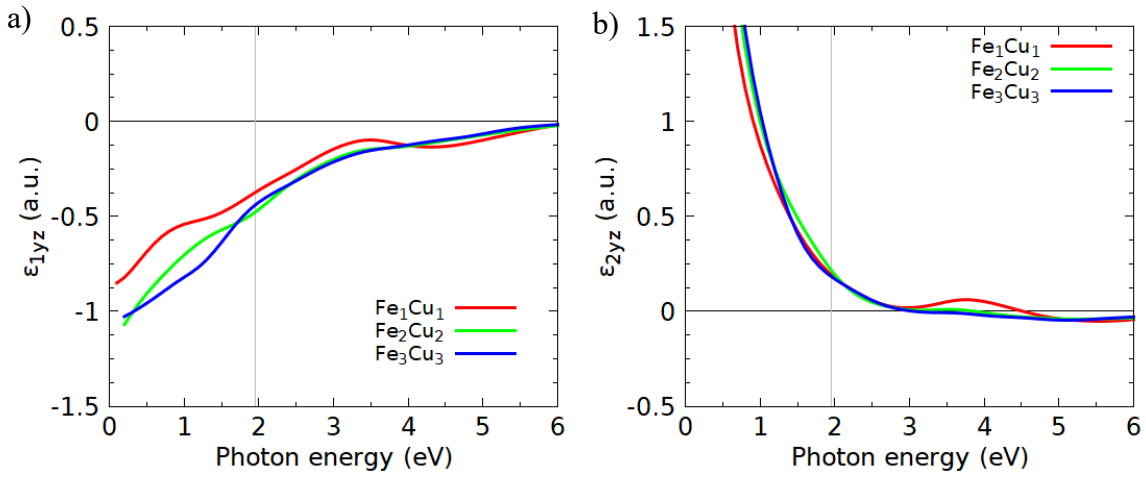

Figure. 4.12: (a) and (b) show the real and imaginary parts of the off-diagonal component ε_{yz} dielectric function of Fe_xCu_x SLs, respectively.

4.5 Optical and magneto-optical anisotropies of the Fe_1Cu_1 SL

In this section, we discuss the electronic origins of the optical and magneto-optical properties (OA and MOA) from first-principles calculations. A OA and MOA may be required for achieving high accuracy in applications [34,41,103], and understanding of optical conductivity in ferromagnetic uniaxial materials with frequency in visible and infrared range is essential. The OA was then estimated by the difference in the real parts of diagonal components, $\sigma_{1xx}-\sigma_{1zz}$, for M_z, and the MOA was given by the difference in the imaginary parts of off-diagonal components for M_z and M_x, $\sigma_{2xy}-\sigma_{2yz}$.

4.5.1 Optical conductivity

The optical conductivities as a function of the photon energy ω up to 6.0 eV are summarized in Fig. 4.13. The absorptive parts, σ_{1xx} and σ_{1zz}, behave differently each other, which exhibit the system with a strong OA, as shown in Figs. 4.13(a) and 4.13(c). The dispersive parts of diagonal components, σ_{2xx} and σ_{2zz}, are negative in low ω and increase

as ω increases, as seen in Fig. 4.13(b). The σ_{1xx} shows large finite values in the whole ω due to the metallic character, where typically two prominent peaks at around 1.5 and 3.5 eV were observed, which are close to those in the previous calculations, 1.6 and 3.4 eV. [104] In the case of σ_{1zz}, although it shows the same trend to that in the σ_{1xx} spectrum, the magnitudes of the two prominent peaks are differently suppressed, namely, the σ_{1zz} peak at 1.5 eV is suppressed significantly but that at 3.5 eV is slight. This makes different features around 1.5 and 3.5 eV in the OA spectrum; the former gives a peak but the latter is a dip, as indicated by vertical arrows in Fig. 4.13(c).

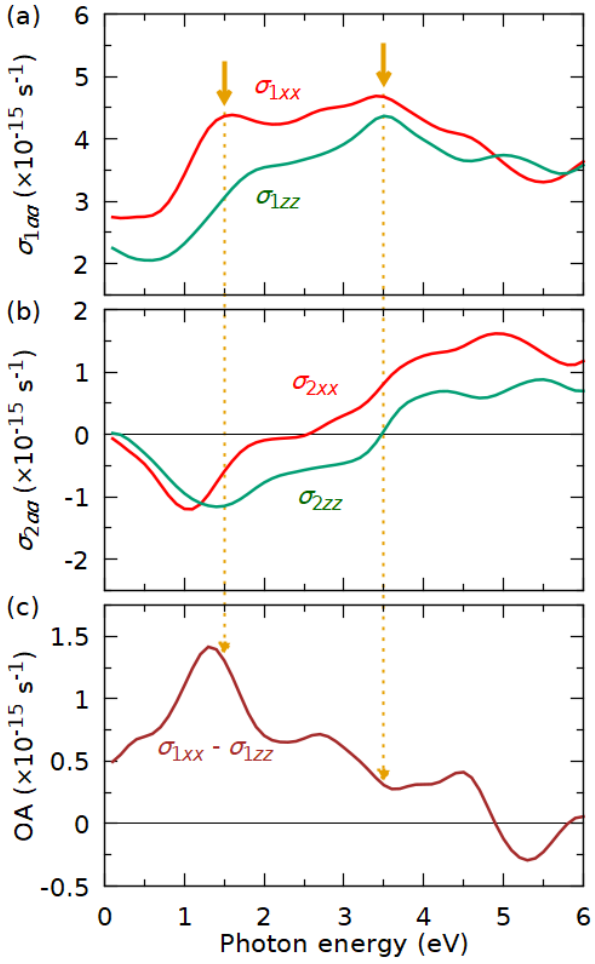

Figure 4.13: Calculated optical spectra of Fe_1Cu_1 SL. (a) and (b) show real and imaginary parts of the diagonal components in optical conductivities for M_z, and (c) shows the OA. Arrows in (a) indicates the prominent features in these spectra.

In the off-diagonal components, the dispersive parts, σ_{1xy} and σ_{1yz}, decrease as ω increases, as shown in Fig. 4.14(a). The typical peaks and shoulders of the absorptive parts, σ_{2xy} and σ_{2yz}, are indicated by vertical arrows in Fig. 4.14(b) with three features at

0.5, 1.7 and 2.5 eV; a valley goes a hump, a peak becomes broad, and a dip changes a broad peak, from σ_{2xy} to σ_{2yz}, respectively. Thus, the MOA at the infrared and visible region is featured by the three peaks at 0.5, 1.7, and 2.5 eV, which exhibit an oscillating behavior with extreme values at these ω positions as seen in Fig. 4.14(c).

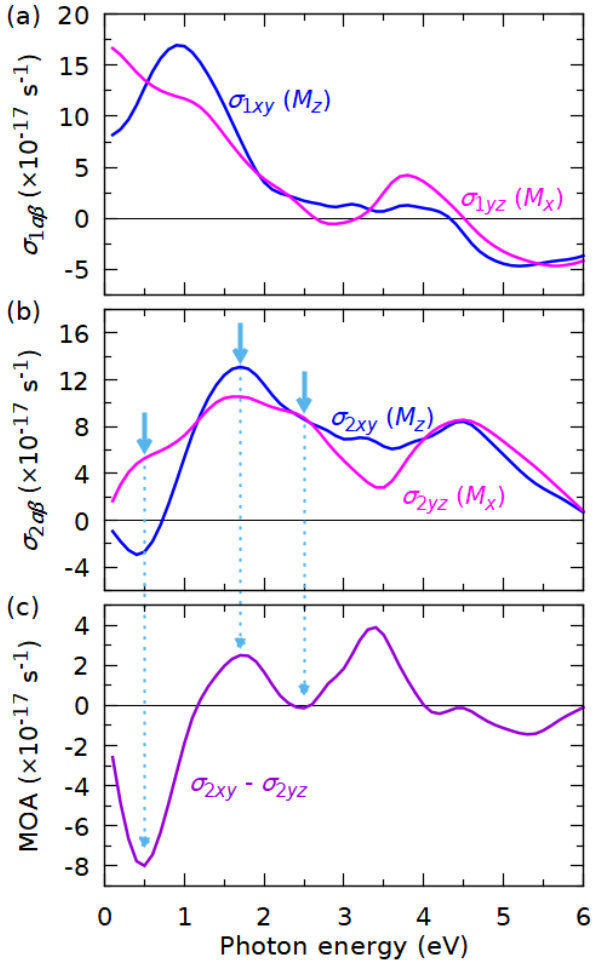

Figure 4.14: (a) and (b) show real and imaginary parts of the off-diagonal components for both M_z and M_x, and (c) shows the MOA. Arrows in (e) indicates the prominent features in these spectra.

4.5.2 Band-by-band decomposition analysis

In order to identify the governed interband transitions in the OA and MOA spectra, we carried out band-by-band decomposition analysis [105,106] to the $\sigma_{1\alpha\alpha}$ and $\sigma_{2\alpha\beta}$ by slicing two bands occupied and unoccupied. In this analysis, as shown in Fig. 4.15, bands are assigned by indexes at each **k**-point by using sequential numbers, N_s, from the lowest energy to above. Figures 4.16(a-b) show the interband contributions to the σ_{1xx} and σ_{1zz} as a function of ω, where a set of the two indexes for initial and final states, $N_i \rightarrow N_f$, is

appended. In the σ_{1xx}, two interband transitions, 19→21 and 19→22, provide a peak at 1.5 eV. In the case of σ_{1zz}, in contrast, the shoulder at 1.5 eV in Fig. 4.14(a) is from 17→20 transition. However, the other set of interband transitions cannot be ruled out in participation to the σ_{1xx} and σ_{1zz} spectra, it is evident that the interband contributions to the σ_{1zz} at 1.5 eV have lower magnitude than those in the σ_{1xx}, which leads to the large OA as seen in Fig. 4.14(c).

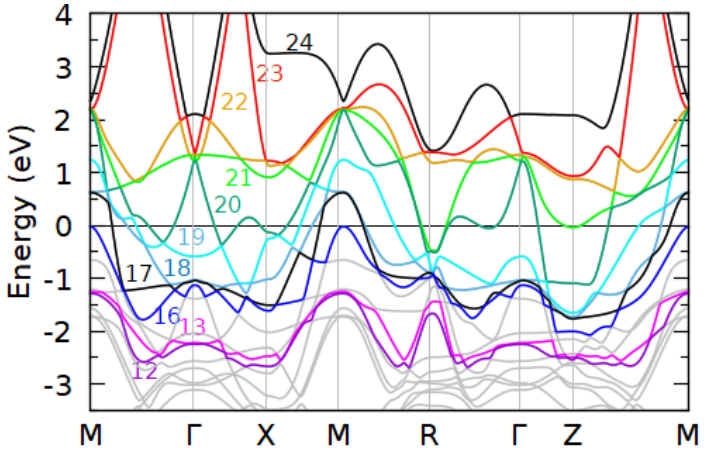

Figure 4.15: Band indexes used in band-by-band decomposition analysis.

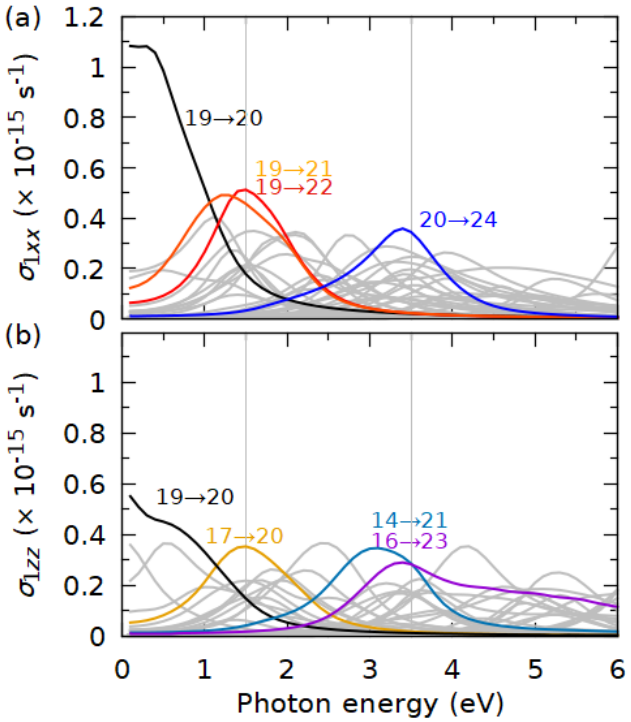

Figure 4.16: Contributions of different interband transitions in (a) σ_{1xx}, and (b) σ_{1zz}, where a set of the two indexes for the initial and final states are represented by N_i→N_f. Vertical grey lines show energy positions of the prominent peaks in the corresponding OA spectrum.

Although the interband contributions to the σ_{1xx} and σ_{1zz} distribute over the whole *k*-space, the contribution along *M*-Γ-*X*-*M*-*R*-Γ-*Z*-*M* path to the interband transitions in the spectra can be assigned. Based on the selection rules and the fat band plot for the Fe *d* orbitals with the minority-spin states, for example, at 1.5 eV, the interband transition of 19→22 around ⅓(*X*-*M*) in the σ_{1xx} correspond to that from Fe $d_{m_z=\pm2}$ to $p_{m_z=\pm1}$ with Δm_z=±1. The final states of 22, which locates at around 1.1 eV above E_F is the antibonding state in the in-plane Fe-Fe *dd* hybridization, and the $p_{m_z=\pm1}$ orbitals in the initial state 19, located about 0.5 eV below E_F, couples to the bonding state of the in-plane Fe-Fe *dd* state through the *pd* hybridization. Meanwhile, the interband transition of 19→21 around ⅓(Γ-*X*) correspond to that from Fe $d_{m_z=\pm1}$ to $p_{m_z=0}$ with Δm_z=±1. In the σ_{1zz}, however, the 19→22 and 19→21 transitions are unallowed due to the different rule of Δm_z=0, and thus the hump in the σ_{1zz} spectra at 1.5 eV in Fig. 4.14(a) is explained by a suppression of the two interband (19→22 and 19→21) transitions. In addition, other contributions come from the interband transition of 17→20 around ½(*M*-*R*) correspond to that from Fe $d_{m_z=\pm1}$ to $p_{m_z=\pm1}$ with Δm_z=±1.

At 3.5 eV, the interband transition of 20→24 in the σ_{1xx} contributes from Fe $p_{m_z=\pm1}$ to $d_{m_z=0,\pm2}$ at around *X* with Δm_z=±1. The final states of 24 located at 3.2 eV are the flat band of $d_{z^2-y^2,xy}$ orbitals that form the small peak of DOS at Fe minority state, as seen in Fig. 4.4(a). In the σ_{1zz}, however, although the interband transition is unallowed due to Δm_z=0, the other interband transitions, e.g., 16→23 (Fe $d_{m_z=\pm1}$ to $p_{m_z=\pm1}$) at ½(*M*-*R*), participate to the σ_{1zz} spectra. Since the initial states of 16 are composed of the Fe $d_{xz,yz}$ orbitals that couple to the Cu *d* orbitals, the peak in the σ_{1zz} at 3.5 eV in Fig. 4.13(a) causes the Fe-Cu *dd* hybridization.

For the off-diagonal components, the interband transitions responsible for the prominent peaks at 0.5 eV in the MOA spectrum can be demonstrated by band-by-band decomposition analysis, as shown in Figs. 4.17(a) and 4.17(b), respectively. At 0.5 eV, the interband transition 19→20 provides a large negative contribution to the σ_{2xy} spectrum but it turns to be positive in the σ_{2yz} spectrum; the former is dominated by the LCP transition, but the latter is by the RCP transition. In the analysis, the 19→20 at ½(*Z*-*M*) corresponds to the transition from $p_{m_z=+1}$ to $d_{m_z=0}$ in the σ_{2xy} but it transforms that from

$p_{m_x=+1}$ to $d_{m_x=+2}$ in the σ_{2yz}, both give different polarizations, RCP and LCP, respectively.

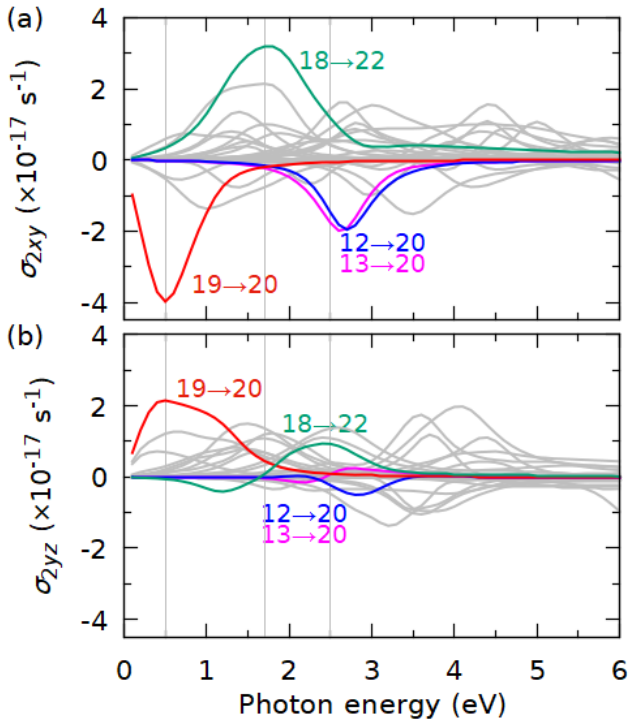

Figure 4.17: Contributions of different interband transitions in (a) σ_{2xy}, and (b) σ_{2yz}. Vertical grey lines show energy positions of the prominent peaks in the corresponding a MOA spectrum.

4.6 Summary

The electronic and optical properties of the Fe_xCu_x SLs are calculated by performing the FLAPW method. We found that the interband transition at peaks in optical conductivity spectra, which is responsible for optical losses, can be tuned through the hybridization process by varying the thickness of the superlattices. The blue and red-shift of the optical conductivity spectrum correspond to the peaks of DOS of Fe minority states. In the visible range, FeCu SLs shows plasmonic properties indicated by negative real part of diagonal component of dielectric function, and MO properties indicated by non-zero off-diagonal component so that it can be offered as magnetoplasmonic in the MOSPR application. In particular, OA and MOA properties of optical conductivity were shown in Fe_1Cu_1 SL. Based on the band-by-band decomposition analysis, the interband transition at 1.5 eV on the OA spectrum is attributed to the strong in-plane Fe-Fe *dd* hybridization. The MOA spectrum is featured by the three prominent peaks at 0.5, 1.7, and 2.5 eV for the off-diagonal components.

Chapter 5

Magneto-optical surface plasmon resonance sensor

5.1 Introduction

Magneto-optical surface plasmon resonance (MOSPR) sensor is a new modulation technique based on MO and SPR interaction. The MOSPR sensor has been proposed and experimentally demonstrated to extremely enhance the performance of the sensor. Substrates as the sensing layer play an essential role in achieving enhanced sensitivity. Combinations of ferromagnetic and noble metals, e.g., (Fe, Co, or Ni)/(Cu, Ag, or Au) multilayer, can be used to enhance both MO effect and SPP excitation.

This chapter demonstrated the MOSPR system in the Kretschmann configuration with FeCu SL using a magnetoplasmonic structure for refractive index detection. To describe the sensitivity of the MOSPR sensor, we first consider the TMOKE and SPP excitation conditions. We exploit the Fe_xCu_x SLs to provide giant TMOKE ($\approx \pm 1$). Then, we present that Fe_xCu_x SLs can increase the sensitivity in the MOSPR system compared to the SPR system.

5.2 Computational methods

The model in the present study is schematically presented in Fig 5.1. We consider the MOSPR systems illuminated by light with the fixed wavelength of λ= 632.8 nm (1.96 eV) through a half-cylindrical glass (BK7, n = 1.515) prims in the Kretschmann configuration. The magnetoplasmonic structure consists of the Fe_xCu_x SLs covered by an Au thin film (d = 1 nm) which is used to prevent oxidation. The dielectric medium is considered as gelatin, with refractive index n_d = 1.341. The complex dielectric function of Au at 632.8 nm wavelength is -11.740 + i1.2611, while the optical parameter of the Fe_xCu_x SLs is taken from the calculation presented in Table 5.1. Applying magnetization to the magnetoplasmonic structure in the opposite direction will change the sign of the off-diagonal component of the dielectric function, $\varepsilon_{yz}(-\mathbf{M}) = -\varepsilon_{yz}(\mathbf{M})$.

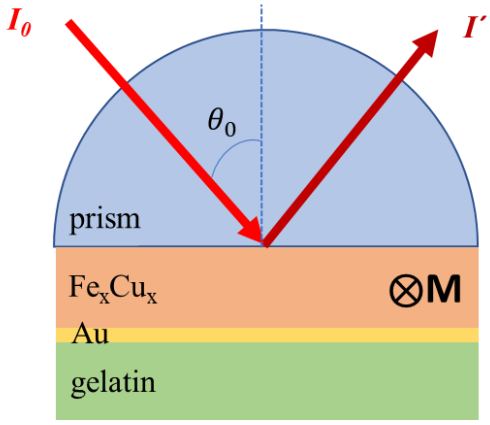

Figure 5.1: Schematic illustration of the Au/Fe_xCu_x MOSPR sensor in the Kretschmann prism coupling system. The magnetization **M** is applied perpendicular to the incident plane.

Table 5.1 Diagonal and off-diagonal of dielectric function of Fe_xCu_x SLs at λ = 1.96 eV.

Superlattices	$\varepsilon_{xx} = \varepsilon_{1xx} + i\varepsilon_{2xx}$	$\varepsilon_{yz} = \varepsilon_{1yz} + i\varepsilon_{2yz}$
Fe_1Cu_1	-7.9025+18.0226i	-0.3725+0.19001i
Fe_2Cu_2	-7.9504+18.9619i	-0.4763+0.2126i
Fe_3Cu_3	-8.6026+19.8839i	-0.4376+0.1810i

The magnitude of TMOKE signal (ΔR/R) is defined through Eq. (2.27). TMOKE measures the differences in the reflectivity when the magnetization is reversed from positive (negative) to negative (positive) sense, along the direction perpendicular to the plane of polarization of the incident light. The reflectivity (R_{pp}) was performed via the 4 × 4 transfer-matrix methods in the form of Eq. (2.44).

5.3 Application to refractive index sensor

5.3.1 Transverse magneto-optical Kerr effect signal

To investigate the reflectivity as a function of the function of incident angle (θ) and thickness (d), we calculated the reflectivity minimum (R_{min}) for θ varying from 60° to 85°, in step of Δθ = 0.01°, and for d = 0 to 40 nm, in step of Δd = 0.01 nm. For visualization purposes, results are presented in Fig. 5.2 by the reflectivity versus both incident angle and thickness of the Fe_xCu_x SLs. A minimum reflectivity around the incident angle of 75 is observed with a white plus sign (+) at the middle of the blue area. The optimum

thicknesses of the Fe_xCu_x SLs are 20.8, 20.3, and 19.7 nm for x =1, 2, and 3, respectively. The different optimum thicknesses for SPP excitation at Fe_xCu_x SLs are due to the different optical absorption determined by the imaginary part of the diagonal dielectric function. In the present simulation, we used a thickness of 19.7 nm to analyze the dependence of optical absorption on the sensitivity of the MOSPR system.

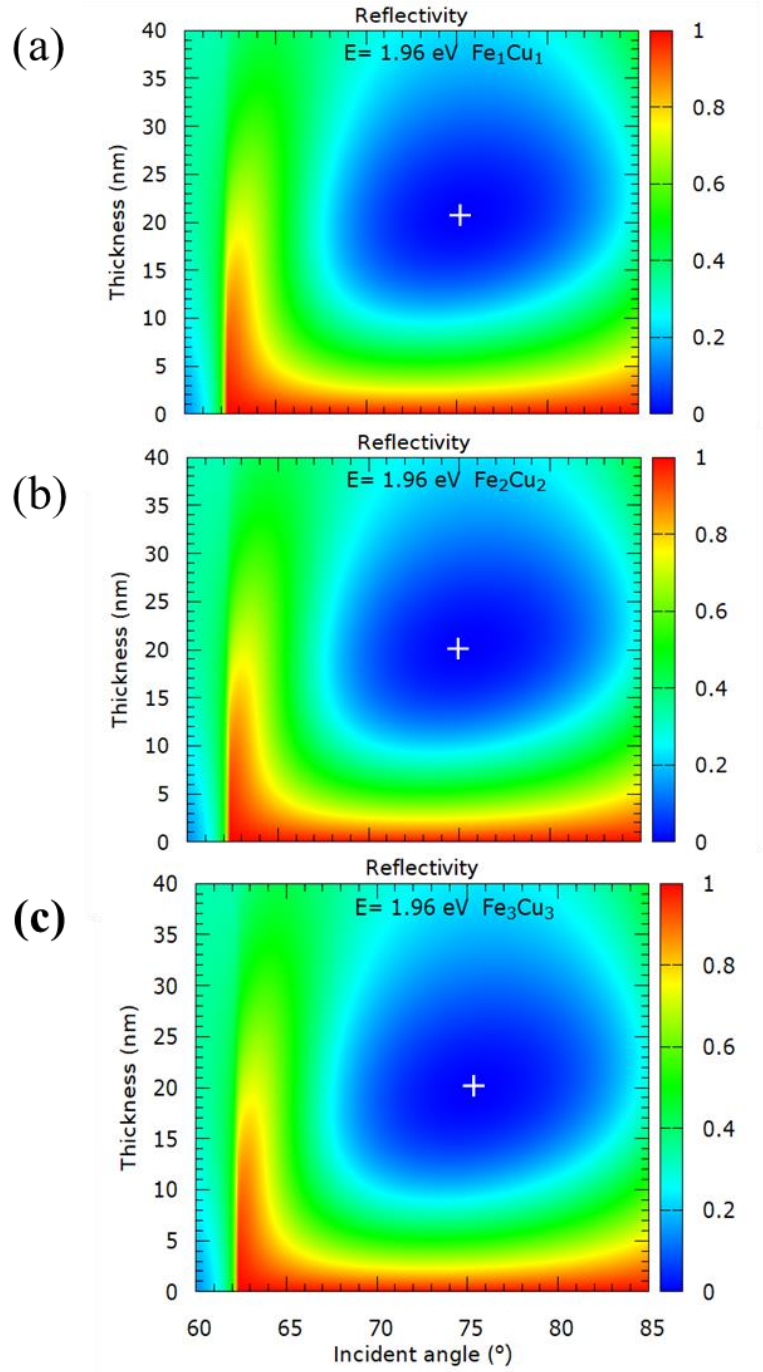

Figure 5.2: Reflectivity as a function of incident angle and thickness for (a) Fe_1Cu_1, (b) Fe_2Cu_2 SL, and (c) Fe_3Cu_3 SLs.

Simulation of R and $\Delta R/R$ in the Kretschmann configuration as a function of incident angle for Fe_xCu_x SLs are shown in Fig. 5.3(a). As expected, the Fe_xCu_x SLs do not exhibit a sharp reflectivity minimum compared to pure noble metals films, since Fe_xCu_x SLs has higher optical absorption characterized by a higher value of the imaginary part of the dielectric function. The reflectivity curve of Fe_xCu_x SLs have an FWHM of 19.1°, indicating a narrowing compared to pure Fe of 20.2°. The SPR angles (θ_{SPR}), which is an excitation of SPP occurs, are 75.24°, 75.42°, and 75.39° for x =1, 2 and 3, respectively, is close to the previous experimental result of the conventional SPR in the Kretschmann configuration for gelatin of 75.4°. [30] In the MOSPR, in contrast, there are strongly enhanced $\Delta R/R$ around θ_{SPR}. Also, for a larger incident angle away from $\theta_{SPR,}$ the magnitude $\Delta R/R$ decreases dramatically. The maximum slope of $d(\Delta R/R)/d\theta$ is 0.31, 1.00, and 12.23 /degree and $dR/d\theta$ of 0.13, 0.13 and 0.14 /degree for x = 1, 2, and 3, respectively, indicating two order magnitude of slope of $\Delta R/R$ compared to R spectra for the Fe_3Cu_3 SL. Using the optimum thickness of 18.9 nm, $d(\Delta R/R)/d\theta$ dan $dR/d\theta$ for pure Fe film are 8.44 and 0.12 /degree, respectively.

The origin of a strong $\Delta R/R$ under SPP excitation is due to both a simultaneous reduction in the reflectivity and an enhancement of the electromagnetic field at the MO active layer. [33,34]

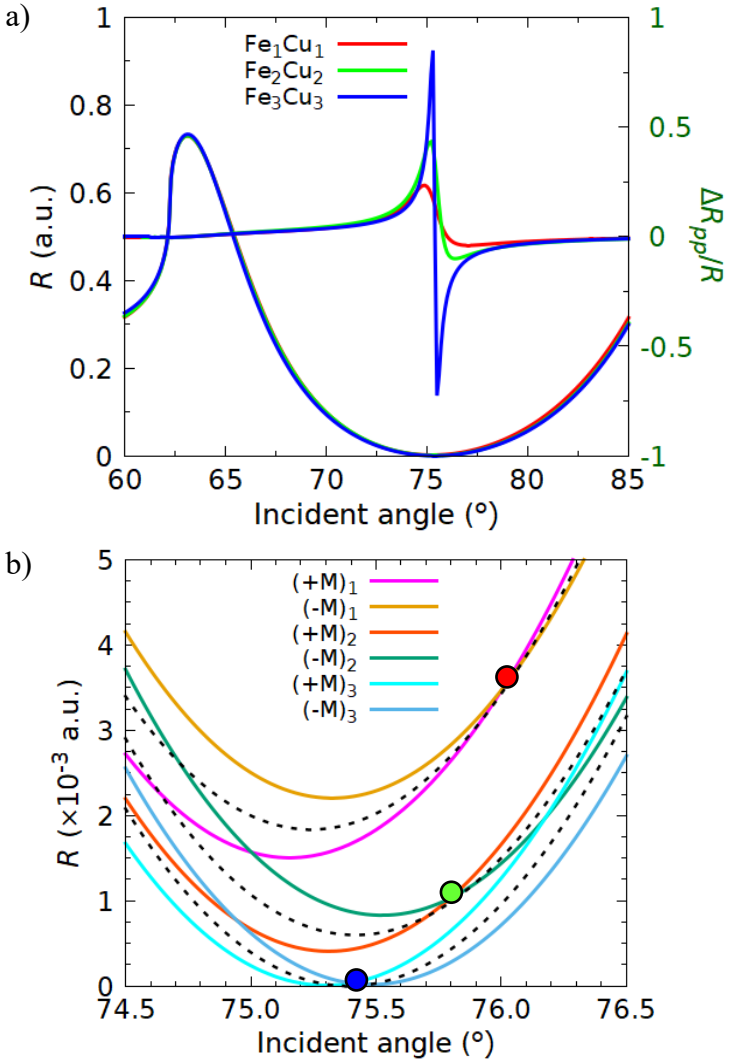

Figure 5.3: (a) Simulated angular spectrum of R and $\Delta R_{pp}/R$ of Fe_xCu_x SLs with the gelatin (n_d = 1.341). (b) The minimum reflectivity $R_{min}(0)$ is marked by dot lines, and the position of zero-crossing of $R(+M)$ and $R(-M)$ is marked by red, green, and blue circles for x = 1, 2, and 3, respectively.

We focus on the dependence of the slope of $\Delta R/R$ on the reflectivity. In fact, when the magnetization is applied perpendicular to the SPP propagation direction, the SPP wave vector can be modified and has nonreciprocal behavior: $\vec{k}_{spp}(+M) \neq \vec{k}_{spp}(-M)$. Consequently, the resonance condition also changes, and the SPR angle is shifted compared with that without magnetization. Figure 5.3(b) shows the minimum of reflectivity without magnetization applied, $R_{min}(0)$, as indicated by dashed lines, and the angular shift of the reflectivity minimum due to the positive and negative applied magnetization, $\Delta\theta = \theta_{min}(+M) - \theta_{min}(-M)$. The present results show $R_{min}(0)$ are 1.84×10^{-3}, 0.59×10^{-3}, and 0×10^{-3} a.u., and $\Delta\theta$ are 0.17, 0.21 and 0.18 degree for x = 1, 2, and 3,

respectively. The magnitude $\Delta\theta$ of FeCu SLs is more significant than that of AuAgCoAg [33] or AuCoAu [107] multilayer on the order of 10^{-2} degree. The $\Delta\theta$, which is also called the modulation factor, is proportional to the Voigt parameter, $Q = i\varepsilon_{yz}/\varepsilon_{xx}$, i.e., 0.0212, 0.0254 and 0.0219 for for x = 1, 2 and 3, respectively. It can be said that the dependence of the slope of $\Delta R/R$ on $\Delta\theta$ is not so significant.

Meanwhile, the shift of reflectivity minimum for the positive and negative applied magnetization, $R_{min}(+)$ and $R_{min}(-)$, respectively, with respect to $R_{min}(0)$, is inversely proportional to the increasing value of x. The position of zero-crossing for $\Delta R/R$, when $R_{pp}(+M) = R_{pp}(-M)$, indicated by dot color in Fig. 5.3(b). The degree of the shifts with respect to $R_{min}(0)$ are 0.77, 0.38 and 0.01 degree for for x = 1, 2, and 3, respectively. Therefore we can conclude that strong $\Delta R/R$ occurs when both the magnitudes of $R_{min}(+M)$ and $R_{min}(-M)$ are equal, and it occurs when R_{min} is close to zero. In other words, the magnitude of $\Delta R/R$ increases drastically with decreasing the R_{min}.

5.3.2 Sensitivity

`One approach to determining the sensitivity of optical sensors is RIU (refractive index units), which is the sensor response on the change of the dielectric refractive index nd. Generally, sensitivity can be defined as [35,108]

$$\eta = \frac{\partial S}{\partial n_d} = \frac{\partial S}{\partial A} \times \frac{\partial A}{\partial n_d}, \tag{5.1}$$

where S represents the R_{pp} (for conventional SPR) or $\Delta R/R$ (for MOSPR) and A is the incident angle of the light. Therefore, the maximum sensitivity will be achieved by combining the high slope of the measured signal as a function of the incident angle and large displacement of the resonance position when nd changes.

To demonstrate our concept for sensing applications, we consider small variations of the refractive index of the gelatin. Figures 5.4(a-c) shows the change of $\Delta R/R$ for the refractive index of gelatin varying from n_d =1.341 to n_d = 1.347, in steps of Δn_d = 0.001. With increasing the refractive index of gelatin, $\Delta R/R$ spectrum gradually shifts to a higher angle due to the larger SPP wavevector.

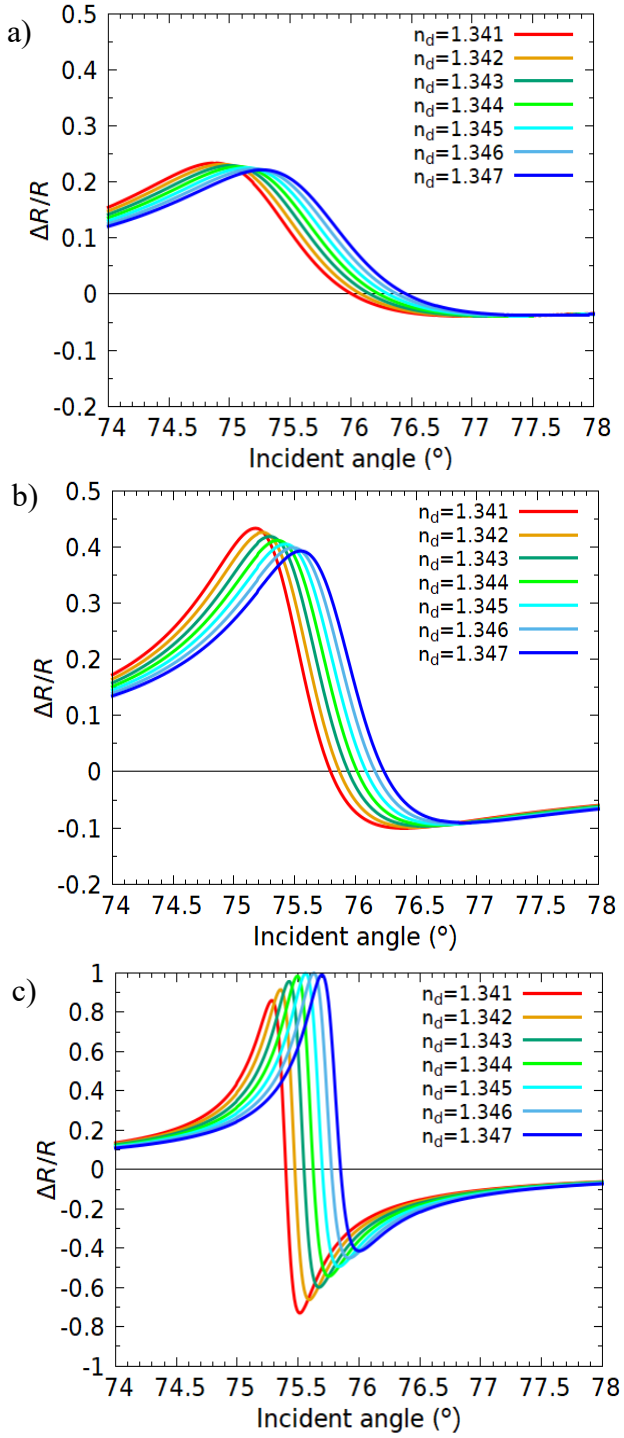

Figure 5.4: Simulated angular spectra of $\Delta R/R$ of (a) Fe_1Cu_1, (b) Fe_2Cu_2, and (c) Fe_3Cu_3 SLs as a function of the index of the gelatin n_d.

The sensitivity can be obtained by Eq. (5.1) and for the MOSPR system shown in Fig. 5.5(a). The numerical calculations predict that the highest sensitivity is 600.1 RIU^{-1} for Fe_3Cu_3 SLs due to the sharp behavior of the $\Delta R/R$, while for the Fe_1Cu_1 and Fe_2Cu_2 SLs, η_1 = 18.8 RIU^{-1} and η_2 = 54.0 RIU^{-1}, respectively, the sensitivity decrease due to the

smaller slope of $\Delta R/R$. The sensitivity of the MOSPR is very sensitive to the number of x. When the x value is less than three, the sensitivity has one order reduction. The higher sensitivity of MOSPR at the Fe_3Cu_3 SL indicates that the tiny change of refractive index can be responded to clearly.

We have additionally simulated the sensitivity of the SPR conventional, and the results are shown in Fig. 5.5(b). In this configuration, the sensitivity of the Fe_xCu_x SLs gives the same magnitude of 8.8 RIU^{-1}, which is two order magnitude lower than the maximum sensitivity of the MOSPR system. We can observe that the shift of θ_{SPR} due to change of n_d in conventional SPR and MOSPR systems is the same.

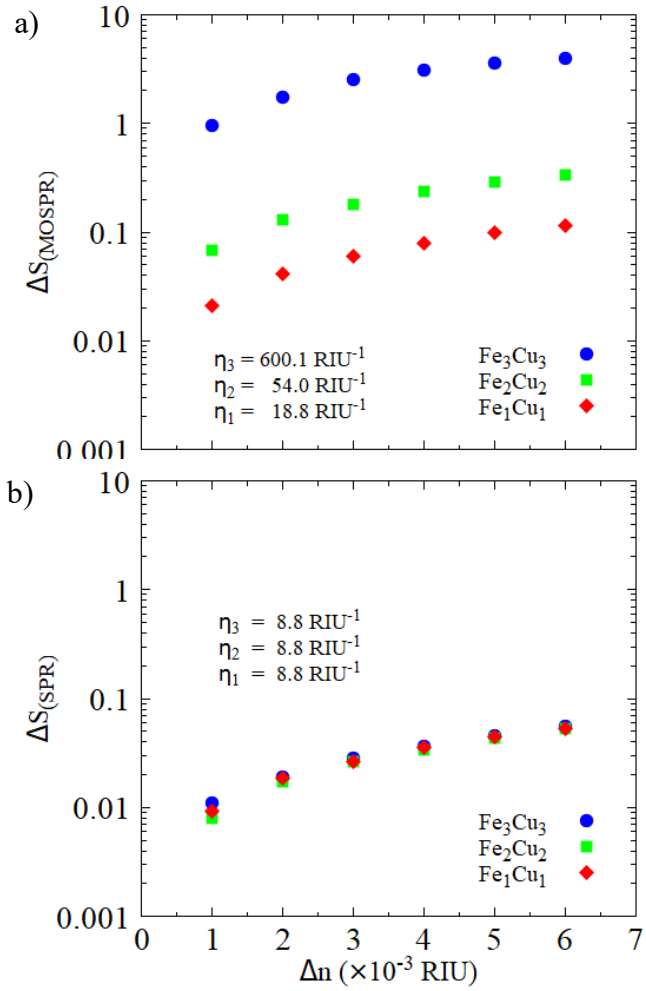

Figure 5.5: Output signal S as function of the refractive index n_d of Fe_xCu_x SLs and pure Fe for the (a) MOSPR and (b) SPR systems.

Although both conventional SPR and MOSPR have different approaches in the measurements, we can conclude that the difference in the sensitivity is dominantly derived from the slope of angular spectra. Therefore, the most important feature of the

MOSPR sensor is a high sensitivity achieved by the giant enhancement of TMOKE signal. We have shown that layer thickness (x) on SLs can tune optical properties and subsequently affect reflectivity curves. By selecting optimized thickness (d), an extremely high slope of TMOKE signal is achieved at the number x of Fe_xCu_x SLs of 3. It is important to point out that the high sensitivity of the MOSPR sensor is performed in the SLs, which is relatively easy to fabricate. It is also shown here that multilayer has advantages over pure ferromagnetic films. Finally, the proposed approach of magnetoplasmonic SLs can be applied to various structures to obtain enhanced sensitivity of the refractive index sensor.

5.4 Summary

This chapter demonstrated the enhancement of the TMOKE signal in Fe_xCu_x SLs. The reflectivity of the structure is studied using 4×4 transfer-matrix methods. Upon comparing the minimum reflectivity with differences in the dielectric function, we could observe the slope feature of the angular spectra. The stronger coupling between surface plasmon and incident wave leads to a sharper TMOKE signal. Then, we have shown TMOKE signal to be sensitive to small changes in the refractive index of the gelatin. The sharp behavior of TMOKE signal is the origin for an enhance in sensitivity. The calculation shows that the sensitivity of the proposed sensor in the MOSPR system is 600.1 RIU^{-1} for Fe_3Cu_3 SL, which is two order magnitude higher than the SPR system of the same configuration. Our result can be implemented for different applications based on the MO effect.

Chapter 6

Conclusions and prospects

In this thesis, we present the study of optical and magneto-optical properties on the magnetoplasmonic material, namely FeCu SLs, by using first-principles calculations for improving the performance of surface plasmon resonance (SPR) application. The basic concept of SPR and magneto-optical SPR (MOSPR) are stated in chapter one.

Chapter two present the theory and method of the electronic structure calculation and magneto-optical Kerr effect (MOKE). We briefly explain the concept of density functional theory (DFT) and full-potential linearized augmented plane wave methods that we apply in present calculations. The optical conductivity tensors that create the link between microscopic theory and macroscopic phenomena of magneto-optical (MO) effect are calculated by applying the Kubo formula in the linear response theory. The reflectivities of multilayer systems are evaluated based on 4×4 transfer matrix method.

Chapter three systematically calculated the optical conductivities and dielectric functions for 3*d* (Fe, Ni, Co, Cu), 4*d* (Ru, Rh, Pd, Ag), and 5*d* (Os, Ir, Pt, Au) transition metals by first-principles calculations. In the optical range, the calculated results are good agreement with experimental data. The edge position of the real part of diagonal optical conductivity for noble metals can be confirmed from the band-by-band decomposition. We also demonstrated the SPR reflectivity curve in the Kretschmann configuration with a sharp dip for noble metals corresponds to a small value of the imaginary part of the dielectric function.

In chapter four, we extend the calculation of electronic structure and optical and MO properties of ferromagnetic/noble metal multilayers, Fe_xCu_x superlattices (SLs) with x = 1, 2, and 3. One of the main physical quantities in magnetoplasmonic is the optical loss caused by the dipole-interband transitions. From calculated electronic structures of Fe_xCu_x SLs, we find that the interband transitions responsible in the optical losses that can be tuned through orbital hybridization by varying the number of layers of the superlattices. In the visible range, Fe_xCu_x SLs are found to have excellent magnetoplasmonic properties, indicated by negative real part of diagonal component of dielectric tensor and by non-zero off-diagonal component, which promise to martial

candidates in the MOSPR applications. In particular, we present the electronic origin in the optical and magneto-optical anisotropies (OA and MOA) of Fe_1Cu_1 SLs based on the band-by-band decomposition analysis.

In chapter five, we implemented Fe_xCu_x SLs to demonstrate the MOSPR system in the Kretschmann configuration by employing the transverse MOKE (TMOKE). Our results show the important role of the minimum reflectivity for the positive and negative applied magnetization on the strength of the TMOKE signal. The maximum slopes of TMOKE signals proportional to the increasing value of *x*. We have demonstrated the TMOKE signal to be sensitive to small variations in the refractive index of the gelatin. The calculation shows that the sensitivity of the MOSPR system for Fe_3Cu_3 SL is two order magnitude higher than the SPR system.

Finally, this dissertation shows an enhanced sensitivity in SPR application as a refractive index sensor using a ferromagnetic/noble metal structure. The combination of materials in the magnetoplasmonic structure promises to establish plasmonic and MO properties, in addition to ease of fabrication. Superlattices offer the advantage that optical properties can be adjusted through a hybridization process of electronic properties. In conclusion, the methodology in this dissertation can open up new opportunities to understand the relationship between optical and electronic properties of the magnetoplasmonic system so that it can be applied in biosensor research.

Bibliography

[1] H. H. Nguyen, J. Park, S. Kang, and M. Kim, Sensors **15**, 10481 (2015).

[2] F. Wu, P. A. Thomas, V. G. Kravets, H. O. Arola, M. Soikkeli, K. Iljin, G. Kim, M. Kim, H. S. Shin, D. V. Andreeva, C. Neumann, M. Küllmer, A. Turchanin, D. De Fazio, O. Balci, V. Babenko, B. Luo, I. Goykhman, S. Hofmann, A. C. Ferrari, K. S. Novoselov, and A. N. Grigorenko, Sci. Rep. **9**, 1 (2019).

[3] P. Si, N. Razmi, O. Nur, S. Solanki, C. M. Pandey, R. K. Gupta, B. D. Malhotra, M. Willander, and A. De La Zerda, Nanoscale Adv. **3**, 2679 (2021).

[4] S. Lee, Y. Sun, Y. Cao, and S. H. Kang, TrAC - Trends Anal. Chem. **117**, 58 (2019).

[5] M. R. Gartia, A. Hsiao, A. Pokhriyal, S. Seo, G. Kulsharova, B. T. Cunningham, T. C. Bond, and G. L. Liu, Adv. Opt. Mater. **1**, 68 (2013).

[6] Y. Zhang, I. D. McKelvie, R. W. Cattrall, and S. D. Kolev, Talanta **152**, 410 (2016).

[7] G. Qiu, Z. Gai, Y. Tao, J. Schmitt, G. A. Kullak-Ublick, and J. Wang, ACS Nano **14**, 5268 (2020).

[8] P. K. Sharma, J. S. Kumar, V. V. Singh, U. Biswas, S. S. Sarkar, S. I. Alam, P. K. Dash, M. Boopathi, K. Ganesan, and R. Jain, Anal. Bioanal. Chem. **412**, 4101 (2020).

[9] A. Ahmadivand, B. Gerislioglu, Z. Ramezani, A. Kaushik, P. Manickam, and S. A. Ghoreishi, Biosens. Bioelectron. **177**, 112971 (2021).

[10] A. Paliwal, A. Sharma, M. Tomar, and V. Gupta, J. Appl. Phys. **119**, (2016).

[11] J. S. Weerakkody, S. Brenet, T. Livache, C. Herrier, Y. Hou, and A. Buhot, J. Phys. Chem. C **124**, 3756 (2020).

[12] Y. Wang, Z. Ye, C. Si, and Y. Ying, Food Chem. **136**, 1303 (2013).

[13] S. Y. Tseng, S. Y. Li, S. Y. Yi, A. Y. Sun, D. Y. Gao, and D. Wan, ACS Appl. Mater. Interfaces **9**, 17306 (2017).

[14] J. Zhou, Q. Qi, C. Wang, Y. Qian, G. Liu, Y. Wang, and L. Fu, Biosens. Bioelectron. **142**, 1 (2019).

[15] J. F. Masson, ACS Sensors **2**, 16 (2017).

[16] N. Bellassai, R. D'Agata, V. Jungbluth, and G. Spoto, Front. Chem. **7**, 1 (2019).

[17] S. A. Maier, *Plasmonics: Fundamentals and Applications* (Springer, New York, 2007).

[18] J. Homola, Chem. Rev. **108**, 462 (2008).

[19] E. Kretschmann and H. Raether, Zeitschrift Fur Naturforsch. - Sect. A **23**, 2135 (1968).

[20] B. Liedberg, C. Nylander, and I. Lunström, Sensors and Actuators **4**, 299 (1983).

[21] Y. B. Shin, H. M. Kim, Y. Jung, and B. H. Chung, Sensors Actuators, B Chem. **150**, 1 (2010).

[22] H. Y. Chung, C. C. Chen, P. C. Wu, M. L. Tseng, W. C. Lin, C. W. Chen, and H. P. Chiang, Nanoscale Res. Lett. **9**, 1 (2014).

[23] S. Suherman, K. Morita, and T. Kawaguchi, Appl. Surf. Sci. **332**, 229 (2015).

[24] G. Kaur, A. Paliwal, M. Tomar, and V. Gupta, Biosens. Bioelectron. **78**, 106 (2016).

[25] B. A. Prabowo, R. Y. L. Wang, M. K. Secario, P. T. Ou, A. Alom, J. J. Liu, and K. C. Liu, Biosens. Bioelectron. **92**, 186 (2017).

[26] J. Qin, Y. Zhang, X. Liang, C. Liu, C. Wang, T. Kang, H. Lu, L. Zhang, P. Zhou, X. Wang, B. Peng, J. Hu, L. Deng, and L. Bi, ACS Photonics **4**, 1403 (2017).

[27] J. Ashley, Y. Shukor, R. D'Aurelio, L. Trinh, T. L. Rodgers, J. Temblay, M. Pleasants, and I. E. Tothill, ACS Sensors **3**, 418 (2018).

[28] W. M. E. M. M. Daniyal, Y. W. Fen, N. A. A. Anas, N. A. S. Omar, N. S. M. Ramdzan, H. Nakajima, and M. A. Mahdi, RSC Adv. **9**, 41729 (2019).

[29] P. Mrozek, E. Gorodkiewicz, P. Falkowski, and B. Hościło, Sensors **21**, 1 (2021).

[30] D. P. Wardani, M. Arifin, E. Suharyadi, and K. Abraha, in *Optical Sensors 2015*, Vol. 9506 (2015), p. 95060W.

[31] M. Arifin, F. D. Laksono, S. Supardianningsih, and K. Abraha, J. Phys. Theor. Appl. **1**, 108 (2017).

[32] D. P. Wardani, M. Arifin, and K. Abraha, in *Materials Science Forum*, Vol. 948 MSF (2019), pp. 146–152.

[33] E. Ferreiro-Vila, J. B. González-Díaz, R. Fermento, M. U. González, A. García-Martín, J. M. García-Martín, A. Cebollada, G. Armelles, D. Meneses-Rodríguez, and E. M. Sandoval, Phys. Rev. B **80**, 125132 (2009).

[34] G. Armelles, A. Cebollada, A. García-Martín, and M. U. González, Adv. Opt. Mater. **1**, 10 (2013).

[35] B. Sepúlveda, A. Calle, L. M. Lechuga, and G. Armelles, Opt. Lett. **31**, 1085 (2006).

[36] D. Regatos, D. Fariña, A. Calle, A. Cebollada, B. Sepúlveda, G. Armelles, and L.

M. Lechuga, J. Appl. Phys. **108**, 054502 (2010).

[37] E. Ferreiro-Vila, M. Iglesias, E. Paz, F. J. Palomares, F. Cebollada, J. M. González, G. Armelles, J. M. García-Martín, and A. Cebollada, Phys. Rev. B **83**, 205120 (2011).

[38] S. Tomita, T. Suwa, P. Riego, A. Berger, N. Hosoito, and H. Yanagi, Phys. Rev. Appl. **11**, 064010 (2019).

[39] C. Rizal, P. O. Kapralov, D. Ignatyeva, V. Belotelov, and S. Pisana, J. Phys. D. Appl. Phys. **53**, (2020).

[40] L. Li, X. Zong, and Y. Liu, Photonics Res. **8**, 1742 (2020).

[41] E. Moncada-Villa, O. N. Oliveira, and J. R. Mejía-Salazar, Phys. Rev. B **102**, 165304 (2020).

[42] Q. Wang, H. Yao, Y. Feng, X. Deng, B. Yang, D. Xiong, M. He, and W. Zhang, Opt. Express **29**, 10546 (2021).

[43] D. A. Garfinkel, G. Pakeltis, N. Tang, I. N. Ivanov, J. D. Fowlkes, D. A. Gilbert, and P. D. Rack, ACS Omega **5**, 19285 (2020).

[44] F. Freire-Fernández, R. Mansell, and S. Van Dijken, Phys. Rev. B **101**, 054416 (2020).

[45] Richard M. Martin, *Electronic Structure: Basic Theory and Practical Methods* (Cambridge University Press, Cambridge, 2004).

[46] P. Hohenberg and W. Kohn, Phys. Rev. **136**, (1964).

[47] W. Kohn and L. J. Sham, Phys. Rev. **140**, (1965).

[48] J. C. Slater, Phys. Rev. **51**, 846 (1937).

[49] O. K. Andersen, Phys. Rev. B **12**, 3060 (1975).

[50] D. D. Koelling and G. O. Arbman, J. Phys. F Met. Phys. **5**, 2041 (1975).

[51] D. R. Hamann, Phys. Rev. Lett. **42**, 662 (1979).

[52] E. Wimmer, H. Krakauer, M. Weinert, and A. J. Freeman, Phys. Rev. B **24**, 864 (1981).

[53] S. Blügel and G. Bihlmayer, in *Computational Nanoscience*, Vol. 31 (John von Neumann Institute for Computing, Julich, 2006), pp. 85–129.

[54] K. Nakamura, T. Ito, A. J. Freeman, L. Zhong, and J. Fernandez-de-Castro, Phys. Rev. B **67**, 014420 (2003).

[55] J. Kerr, Philos. Mag. J. Sci. **3**, 321 (1877).

[56] M. G. Manera, A. Colombelli, A. Taurino, A. G. Martin, and R. Rella, Sci. Rep. **8**, 12640 (2018).

[57] Q. Gui, Y. Zhou, S. Liao, Y. He, Y. Tang, and Y. Wang, Soft Matter **15**, 393 (2019).

[58] T.-Y. Tsai, T.-Y. Chen, C.-T. Wu, H.-I. Chan, and C.-F. Pai, Sci. Rep. **8**, 5613 (2018).

[59] H. Shibata, M. Okano, and S. Watanabe, Phys. Rev. B **97**, 014438 (2018).

[60] J. Zak, E. R. Moog, C. Liu, and S. D. Bader, Phys. Rev. B **43**, 6423 (1991).

[61] M. Dresselhaus, G. Dresselhaus, S. B. Cronin, and A. G. S. Filho, *Solid State Properties: From Bulk to Nano* (Springer-Verlag Berlin Heidelberg, Berlin, 2018).

[62] C. Kittle, *Introsuction to Solid State Physics*, 8th ed. (John Wiley & Sons, USA, 2005).

[63] H. S. Bennett and E. A. Stern, Phys. Rev. **137**, A448 (1965).

[64] P. M. Oppeneer, T. Maurer, J. Sticht, and J. Kübler, Phys. Rev. B **45**, 924 (1992).

[65] H. Ebert, Reports Prog. Phys. **59**, 1665 (1996).

[66] L. Uba, S. Uba, and V. N. Antonov, Phys. Rev. B **96**, 235132 (2017).

[67] S. Uba, L. Uba, A. Yaresko, A. Y. Perlov, and V. Antonov, Phys. Rev. B **53**, 6526 (1996).

[68] P. Bruno, Y. Suzuki, and C. Chappert, Phys. Rev. B **53**, 9214 (1996).

[69] J. Hamrle, Magneto-Optical Determination of the in-Depth Magnetization Profile in Magnetic Multilayers, Université Paris Sud - Paris XI, 2003.

[70] P. B. Johnson and R. W. Christy, Phys. Rev. B **6**, 4370 (1972).

[71] M. Arifin, T. Matsumoto, A. M. Pradipto, T. Akiyama, T. Ito, and K. Nakamura, E-Journal Surf. Sci. Nanotechnol. **18**, 133 (2020).

[72] J. P. Perdew, K. Burke, and M. Ernzerhof, Phys. Rev. Lett. **77**, 3865 (1996).

[73] R. W. G. Wyckoff, *Crystal Structures*, 2nd ed. (Interscience Publishers, New York, 1963).

[74] V. J. Keast, B. Zwan, S. Supansomboon, M. B. Cortie, and P. O. Å. Persson, J. Alloys Compd. **577**, 581 (2013).

[75] M. Polyanskiy, https://refractiveindex.info/.

[76] H. S. Sehmi, W. Langbein, and E. A. Muljarov, Phys. Rev. B **95**, 115444 (2017).

[77] P. B. Johnson and R. W. Christy, Phys. Rev. B **9**, 5056 (1974).

[78] S. Babar and J. H. Weaver, Appl. Opt. **54**, 477 (2015).

[79] S. Adachi, *The Handbook on Optical Constants of Metals: In Tables and Figures* (2012).

[80] J. H. Weaver, C. G. Olson, and D. W. Lynch, Phys. Rev. B **15**, 4115 (1977).

[81] V. V Nemoshkalenko, V. N. Antonov, and M. M. Kirillova, Zh. Eksp. Teor. Fiz. **90**, 201 (1986).

[82] L. Yan and J. A. Woollam, J. Appl. Phys. **92**, 4386 (2002).

[83] J. H. Weaver, Phys. Rev. B **11**, 1416 (1975).

[84] V. G. Kravets, R. Jalil, Y. J. Kim, D. Ansell, D. E. Aznakayeva, B. Thackray, L. Britnell, B. D. Belle, F. Withers, I. P. Radko, Z. Han, S. I. Bozhevolnyi, K. S. Novoselov, A. K. Geim, and A. N. Grigorenko, Sci. Rep. **4**, 1 (2014).

[85] K. Takagi, S. V. Nair, R. Watanabe, K. Seto, T. Kobayashi, and E. Tokunaga, J. Phys. Soc. Japan **86**, 1 (2017).

[86] P. Arora, E. Talker, N. Mazurski, and U. Levy, Sci. Rep. **8**, 1 (2018).

[87] S. Sundar Manoharan, M. Klaua, J. Shen, J. Barthel, H. Jenniches, and J. Kirschner, Phys. Rev. B **58**, 8549 (1998).

[88] J. Y. Huang, J. Z. Jiang, H. Yasuda, and H. Mori, Phys. Rev. B **58**, R11817 (1998).

[89] H. R. Gong, L. T. Kong, and B. X. Liu, Phys. Rev. B **69**, 1 (2004).

[90] O. I. Gorbatov, I. K. Razumov, Y. N. Gornostyrev, V. I. Razumovskiy, P. A. Korzhavyi, and A. V. Ruban, Phys. Rev. B **88**, 174113 (2013).

[91] A. H. Alami and A. A. Hawili, Appl. Surf. Sci. Adv. **1**, 100027 (2020).

[92] A. Houcher, M. Boukelkoul, S. Benchikh, and M. F. Haroun, J. Magn. Magn. Mater. **512**, 167038 (2020).

[93] S. A. Chambers, T. J. Wagener, and J. H. Weaver, Phys. Rev. B **36**, 8992 (1987).

[94] M. Arifin, K. Nawa, and K. Nakamura, Jpn. J. Appl. Phys. **60**, 092006 (2021).

[95] G. Arfken, *Mathematical Methods for Physicists*, 3rd ed. (Academic Press, California, USA, 1985).

[96] S. F. Cheng, A. N. Mansour, J. P. Teter, K. B. Hathaway, and L. T. Kabacoff, Phys. Rev. B **47**, 206 (1993).

[97] B. K. Wang, G. Y. Guo, and C.-R. Chang, J. Magn. Magn. Mater. **209**, 214 (2000).

[98] J. T. Wang, L. Zhou, Y. Kawazoe, and D. S. Wang, Phys. Rev. B **60**, 3025 (1999).

[99] Z. P. Shi, J. F. Cooke, Z. Zhang, and B. M. Klein, Phys. Rev. B **54**, 3030 (1996).

[100] H. Miyazawa and T. Oguchi, J. Phys. Soc. Japan **68**, 1412 (1999).

[101] K. Nakamura, R. Shimabukuro, Y. Fujiwara, T. Akiyama, T. Ito, and A. J. Freeman, Phys. Rev. Lett. **102**, 187201 (2009).

[102] W. K. Li and G. Y. Guo, Phys. Rev. B **103**, 014439 (2021).

[103] R. Warmbier, G. S. Manyali, and A. Quandt, Phys. Rev. B **85**, 085442 (2012).

[104] A. Djabri, M. Mahdi, R. Boukhalfa, M. Erkovan, Y. Chumakov, and F. Chemam, J. Supercond. Nov. Magn. **30**, 3207 (2017).

[105] L. Uba, S. Uba, V. N. Antonov, A. N. Yaresko, and R. Gontarz, Phys. Rev. B **62**, 16510 (2000).

[106] S. Uba, A. Bonda, L. Uba, L. V. Bekenov, V. N. Antonov, and A. Ernst, Phys. Rev. B **94**, 1 (2016).

[107] J. B. González-Díaz, A. García-Martín, G. Armelles, J. M. García-Martín, C. Clavero, A. Cebollada, R. A. Lukaszew, J. R. Skuza, D. P. Kumah, and R. Clarke, Phys. Rev. B **76**, 153402 (2007).

[108] D. Regatos, B. Sepúlveda, D. Fariña, L. G. Carrascosa, and L. M. Lechuga, Opt. Express **19**, 8336 (2011).

List of Publication

1. Muhammad Arifin, Takahiro Matsumoto, Abdul-Muizz Pradipto, Toru Akiyama, Tomonori Ito, Kohji Nakamura, 'First principles calculation of optical properties of transition metals for surface plasmon resonance application', *e-Journal of Surface Science and Nanotechnology,* **18**, 133-138 (2020).
2. Muhammad Arifin and Kohji Nakamura, 'Optical and magneto-optical properties of Fe_xAg_x superlattices: first-principles study', *Journal of Physics: Conference Series*, **1951** (1), 0120461-7 (2021).
3. Muhammad Arifin, Kenji Nawa, and Kohji Nakamura, 'Optical and magneto-optical anisotropies of FeCu superlattice: band-by-band decomposition analysis', *Japanese Journal of Applied Physics*, **60** (9), 0920061-6 (2021).

List of Presentations

International Conferences

1. Muhammad Arifin, Abdul-Muizz Pradipto, Toru Akiyama, Tomonori Ito, Kohji Nakamura, “Ab initio calculated optical and magneto-optical properties of M/Fe (M=Cu, Ag, Au) superlattices”, *The 80th JSAP Autumn Meeting 2019*, Hokkaido University, Japan, September 18-21, 2019.
2. Muhammad Arifin, Kohji Nakamura, “Transverse magneto-optical Kerr effect of Fe_xCu_x superlattices for surface plasmon resonance application: first principle study”, *The 81th JSAP Autumn Meeting 2020*, Virtual meeting, September 8-11, 2020.
3. Muhammad Arifin, Kohji Nakamura, “Electronic structure and magneto-optical anisotropy of FeCu superlattice: first-principles study”, *The 68th JSAP Spring Meeting 2021*, Virtual meeting, March 16-19, 2021.
4. Muhammad Arifin and Kohji Nakamura, “First-principle studies on magneto-optical anisotropy of Fe_x/Cu_x superlattice”, Bulletin of the American Physical Society, *APS March Meeting 2021*, virtual meeting, March 15–19, 2021.